SINGLE-STEP SYNTHESIS OF THREE-DIMENSIONAL PARTICLES USING NON-UNIFORM UV POLYMERIZATION

By

Navid Hakimi, BSc

Chemical Engineering

Amirkabir University of Technology, Tehran, Iran, 2011

A thesis

presented to Ryerson University

in partial fulfillment of the

requirements for the degree of

Master of Applied Science

in the Program of

Chemical Engineering

Toronto, Ontario, Canada

AUTHOR'S DECLARATION

I hereby declare that I am the sole author of this thesis. This is a true copy of the thesis, including any required final revisions, as accepted by my examiners.

I authorize Ryerson University to lend this thesis to other institutions or individuals for the purpose of scholarly research.

I further authorize Ryerson University to reproduce this thesis by photocopying or by other means, in total or in part, at the request of other institutions or individuals for the purpose of scholarly research.

I understand that my thesis may be made electronically available to the public.

ABSTRACT

Navid Hakimi

SINGLE-STEP SYNTHESIS OF THREE-DIMENSIONAL PARTICLES USING NON-UNIFORM UV POLYMERIZATION

M.A.Sc, Chemical Engineering, Ryerson University, Toronto, 2014

Polymer-based microparticles are increasingly utilized in a range of biotechnology application. There is growing evidence that microparticle shape is an important parameter governing its functionality. Yet, there currently exists no straightforward method to controllably synthesize a large number of highly three-dimensional (3D) microoparticles. In this thesis, we develop a one-step two-dimensional (2D) stop-flow lithography method that exploits the non-uniformity of the polymerizing ultraviolet (UV) light, UV adsorption by opaque nanoparticles in the precursor solution, and discontinuous photomask patterns, to make highly curved 3D microparticles. We investigate the microparticle shape dependence on each parameter by independently tuning the field and focus of the UV light, adding opaque magnetic nanoparticles to the precursor solution, and using a variety of photomask patterns.We also perform numerical simulations of oxygen concentration and monomer conversion in the microfluidic channel, to predict the particle shape.

By simplifying the synthesis of high curvature 3D particles with 3D surface features and branched structures, our method may lead to the expanded use of microparticles in research and in industry.

ACKNOWLEDGMENTS

TABLE OF CONTENTS

List of Tables

List of Figures

NOMENCLATURE and ABERRATIONS

Nomenclature

A	Cross-section area
D_O	Diffusivity of oxygen
F	Focal plane relative distance
H	microchannel height
I	UV light intensity
k_O	Oxidation reaction constant
k_p	Polymerization reaction constant
k_t	Termination reaction constant
$[O_{2,eqb}]$	Equilibrium oxygen concentration
$[OM]$	Opaque material concentration
$[PI]$	Photoinitiator concentration
r_a	Free-radical formation
Re	Reynolds number
T_{Field}	Depth of field
T_{focus}	Depth of focus
$[X]$	Free-radicals concentration

Greek letters

ε_1	Photoinitiator's extinction coefficient
ε_2	Magnetic nanoparticles' extinction coefficient
ζ	Nondimensionalized vertical direction
θ	Contact angel
ξ	Nondimensionalized monomer concentration
ρ	Nondimensionalized radial direction
σ	Nondimensionalized oxygen concentration

τ	Nondimensionalized time
φ	Quentom yield of radical formation
ω_0	Photomask diameter

Aberrations

2D	Two Dimensional
3D	Three Dimensional
CFL	Continuous Flow Lithography
DMD	Digital Mirror Device
ECM	Extracellular Matrix
LRL	Lock-Release Lithograph
MEMs	Micro-Electro-Mechanics
MF	Magnetic Field
MNPs	Magnetic Nanoparticles
N. A.	Numerical Aperture
PFPE	Perfluoropolyether
PET	Poly(ethylene terephthalate)
PRINT	Particle Replication in Non-wetting Templates
SFEP	Surfactant-Free Emulsion Polymerisation
SFL	Stop-Flow Lithography
UV	Ultraviolet

CHAPTER 1

INTRODUCTION

Manufactured microparticles have numerous emerging application areas, namely, in drug delivery(Qiu and Park 2012, 49-60), tissue engineering(Chung et al. 2012, 45-59), particle-assembly(Glotzer and Solomon 2007, 557-562), and microelectromechanical systems (MEMS)(Spearing 2000, 179-196) among others. One of the most important properties of microparticles in their applications is their shape(Lee, Yoon, and Lahann 2011, 195-202). For example, in microparticle-based drug delivery, the shape of the delivery vehicle is an important parameter that determines the diffusion and penetration properties of the drug(Champion, Katare, and Mitragotri 2007, 3-9). In therapeutics and diagnostics applications, a biological event can be enhanced by simply changing the particle shape(Barua et al. 2013, 3270-3275). In microfluidic cell sorting by electromagnetic(Pamme and Wilhelm 2006, 974-980) or acoustic forcing(Franke et al. 2010, 789-794), the living cells being sorted have three-dimensional (3D) features that influence the cell trajectory. The effects of these 3D features get lost in models that only consider the cells as spheres(Tsai, Griffiths, and Stone 2011, 2577-2582)(Tsai et al. 2011). In addition, the controlled self-assembly of non-spherical particles(Tsai et al. 2011) presents expanded possibilities for assembled micromachines(Whitesides and Grzybowski 2002, 2418-2421).

Despite the importance of particle shape, most applications of microparticles still consist of only spherical particles(Das, Zhang, and Kumacheva 2006, 117-142). Two dimensional (2D) particle shapes can be produced using a number of techniques, but making non-spherical particles with 3D features in a reproducible and single-step fashion, and with compatible chemistry has

remained challenging. Bottom-up bulk emulsification techniques are limited to either spherical or spheroidal shapes, and can only produce monodisperse particles using specially chosen materials(Saunders and Vincent 1999, 1-25). Top-down methods, such as femtosecond laser direct writing (FsLDW)(Zhang et al. 2010, 435-448) and multiphoton fabrication(LaFratta et al. 2007, 6238-6258; Laza et al. 2012, 1304-1308) enable highly resolved 3D particles. However, these approaches are prohibitively time-consuming unit operations, and the choice of materials is limited. Particle replication in non-wetting templates (PRINT)(Rolland et al. 2005, 10096-10100) is an alternative multi-step approach for making simple 3D particles, but the range of possible shapes is limited by the mold design.

Microfluidics-based methods for particle synthesis are continuous, and can be multiplexed for higher throughput(Merkel et al. 2010, 13086-13096). Spherical and spheroidal particles(Hwang, Dendukuri, and Doyle 2008, 1640-1647) are attainable in droplet-based microfluidic devices where monodispersed precursor droplets are formed in T-junction(Garstecki et al. 2006, 693-693) or flow-focusing(Shum et al. 2010, 108-118) geometries, and then cured using light or thermal polymerization.

Microfluidic continuous flow lithography (CFL)(Dendukuri et al. 2006, 365-369) techniques also provide a single-step route to synthesize monodispersed particles, with precise control over desired morphologies, and the ability to utilize compatible and functional materials(Helgeson, Chapin, and Doyle 2011, 106-117). An advanced version of CFL is microfluidic stop-flow lithography (SFL)(Dendukuri et al. 2007, 818-828), which has better particle resolution and improved throughput. CFL and SFL are able to produce 2D extruded particles, but controllably synthesizing 3D particles is still difficult with these methods(Dendukuri and Doyle 2009, 4071-4086). Existing flow-lithography based methods such as stop-flow interface

2

lithography(Jang et al. 2007, 9027-9031) and lock release lithography(Bong, Pregibon, and Doyle 2009, 863-866) produce particles with limited 3D features, and often require difficult-to-manufacture 3D channels. To date, single-step synthesis of truly 3D particles from a simple 2D microfluidic channel has not been implemented.

1.1 Objectives

The best method for synthesis of complex particles should produce large quantities of monodispersed particles in designed shapes with the ability to finely tune chemical anisotropy as necessary. Moreover, the process should afford the use of materials that are functionalizable and biocompatible when required.

To our knowledge, a particle synthesis method that combines particle structural and chemical complexity with economical affordability is lacking.

Based on limitations of current microparticle synthesis methods, we set our objectives as:

1. **Develop a flow-lithography based method that is able to generate complex 3D functional particles in a 2D channel.**

2. **Develop a numerical model that is able to predict the synthesized particles' shapes.**

CHAPTER 2

LITERATURE REVIEW

2.1 Introduction

This chapter begins with a brief introduction to polymeric hydrogels. Then, current methods of synthesizing microparticles are reviewed, and their limitations and advantages are summarized.

2.2 Polymeric Hydrogels

2.2.1 Crosslinking polymers

A crosslink bond happens when polymer chain links to another one. These bonds are either covalent bonds or ionic bonds(KRATOCHVfL 1996).

When a synthetic polymer is said to be "crosslinked", it means that the whole bulk of the polymer has been exposed to a crosslinking technique. The resulting modification of mechanical properties depends on the crosslink density. Low crosslink density reduces the viscosities of polymer melts. Intermediate crosslink densities change gummy polymers into materials that have elastomeric properties and possibly high strengths. While very high crosslink densities can make materials very rigid(Gent 2001).

Heat, pressure, change in pH, or radiation such as UV light can initiate chemical reactions that form crosslinked networks. Crosslinked networks are the distinguishing property of thermosetting plastic materials. When polymer chains are linked together by crosslinks, they may

lose some of their ability to move as separated polymer chains. For example, a liquid polymer (where the chains are freely flowing) can be turned into a "solid" or "gel" by crosslinking the chains together. In most cases, crosslinking is permanent. In other words, if heated, the resulting thermosetting substance will destroy or burn, without melting.

Crosslinking density is typically calculated by swelling experiments. A crosslinked polymer is placed into a solvent at a specified temperature, and the change in mass or the change in volume is measured. More crosslinking means less swelling is attainable(Flory and P J. 1953).

2.2.2 Hydrogel particles

By definition, a gel is "nonfluid colloidal network or crosslinked polymer network that is expanded throughout its whole volume by a fluid."(International Union of Pure and Applied Chemistry. Commission on Macromolecular Nomenclature, Jones, and International Union of Pure and Applied Chemistry. Commission on Macromolecular Nomenclature 2009, 443). A gel has a finite, rather small, yield stress. Gel in which the swelling agent is water is called "Hydrogel".

Hydrogels are hydrophilic natural or synthetic polymers. They are highly water absorbent and they can contain over 99.9% water. Hydrogels also possess a degree of flexibility very similar to natural tissue, due to their significant water content. The swelling behavior of microgels is ruled by the unevenness between repulsive and attractive forces. Generally, when ionic repulsion and osmotic forces surpass attractive forces in the polymer network, such as hydrogen bonding, van der Waals interactions, hydrophobic and specific interactions, the hydrogel swells(Das, Zhang, and Kumacheva 2006, 117-142).

PolyHEMA (2-hydroxy-ethyl methacrylate), ethylene glycol dimethacrylate (EDMA), MMA (methylmethacrylate), and isobutyl methacrylateIn are common precursors for hydrogels. In our setup, we used Poly(ethylene)-glycol-diacrylate (PEGDA) as crosslinking agent (**Figure 2-1**). When exposed to UV light in the presence of a photoinitiator, liquid PEGDA can be crosslinked into a gel. Since PEGDA hydrogel is similar to natural tissue, it has found applications in **tissue engineering**(Drury and Mooney 2003, 4337-4351), **cell culture**(Tibbitt and Anseth 2009, 655-663), **drug delivery systems**(Hoare and Kohane 2008, 1993-2007), and **biosensors**(Bryant, Nuttelman, and Anseth 2000, 439-457).
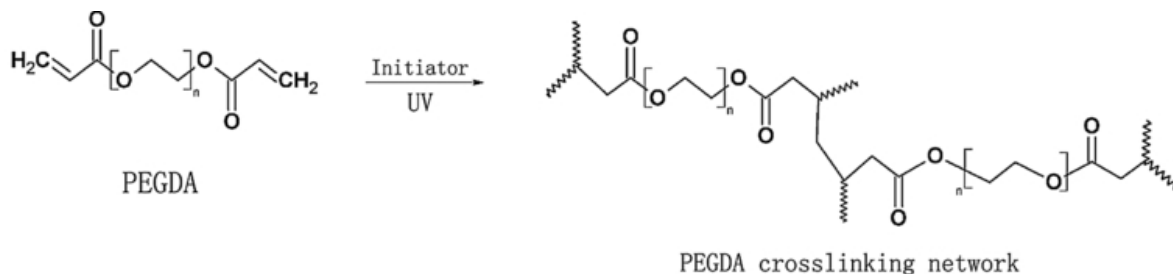
Figure 2-1 Crosslinkg of Polyethylene Glycol Diacrylate

2.2.3 Magnetic Hydrogels

Hydrogels have common applications in biomedical engineering due to their high-water content and tunable properties (e.g., mechanical and chemical) which resemble native extracellular matrix (ECM). However, utilizing hydrogels in modern applications such as engineering 3D tissue blocks and active targeting in drug delivery remain challenging, due to the limitations of controllability, actuation, and quick-response properties(Li et al. 2013, 660-672). Recently, embedding magnetic nanoparticles (MNPs) in hydrogels have emerged as a resourceful

modification for applications that require particles with active responsive properties (Medeiros et al. 2011, 139-161).

Magnetic hydrogels generally consist of a polymer crosslinked matrix and a magnetic component capsulated in the matrix. Hydrogels that are containing MNPs have been verified to be more suitable than those with microsized magnetic particles for biomedical applications in which a quick respond of microparticles to an external stimuli is crucial. The respond of hydrogels containing MNPs to a magnetic field is instantaneous, which displays superparamagnetism. The properties of magnetic hydrogels (e.g., magnetic response) rely on several factors, including the type of MNPs, their concentration, and the size and distribution of the MNPs within the hydrogels(Shin et al. 2008, 12107-12111).

Magnetic microparticles have been explored for many applications. For example, it is confirmed that in tissue engineering, magnetic hydrogel particles can be assembled to form complex 3D tissue structures via a magnetic field. The feasibility of using magnetic hydrogels in drug delivery systems has also been verified(Kost, Wolfrum, and Langer 1987, 1367-1373).

2.2.4 Janus particles

Janus particles are microparticles whose surfaces have two or more distinctive physical or chemical properties (**Figure 2-2**)(Li, Josephson, and Stein 2011, 360-388). For example, a Janus microparticle may have one-half of its surface composed of hydrophilic groups and the other half hydrophobic groups. This feature gives these particles unique and fascinating properties owing to their asymmetric structure and/or functionalization. As a result, Janus particles have emerging applications in self-assembly systems(Walther, Hoffmann, and Müller 2008, 723-726), in

hydrogen peroxide decomposition as catalyst(Ghosh et al. 2013, 268301), water-repellent fibers (Synytska et al. 2011, 1216-1220), and in Micro-Electro-Mechanics (MEMs)(Nisisako et al. 2006, 1152-1156).
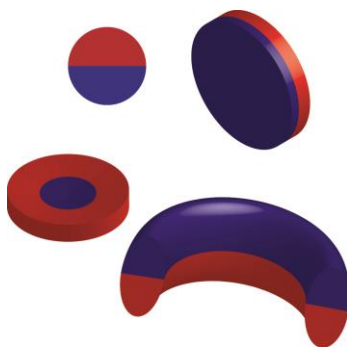
Figure 2-2 Janus Particles

2.3 Free-radical polymerization

The majority of microparticle synthesis methods that are introduced in this thesis as well as our method utilize free-radical polymerization mechanism in order to crosslink the monomer chains. In this section, a brief introduction to free-radical polymerization is described.

Similar to anionic, cationic and coordination polymerization, free-radical polymerization is a type of chain-growth polymerization. In chain-growth polymerization, the equilibrium between polymer and monomers can be illustrated by the thermodynamics of the polymerization. The Gibbs free energy (ΔGp) of the polymerization can usually be used to quantify the inclination of a polymeric reaction. The polymerization will be favored if ΔGp < 0; if ΔGp > 0, the polymer will undergo depolymerization. According to the equation $\Delta G = \Delta H - T\Delta S$, a negative enthalpy and an increasing entropy will move the equilibrium in favorite of polymerization.

In free-radical polymerization, polymers form by the successive addition of free radical building blocks. These free radicals are generated by a number of different mechanisms that

usually involve initiator molecules. Monomer units add to the initiating free radical and result in the growing of polymer chains. Free radical polymerization is commonly used to generate a wide variety of different polymers and material composites. (Odian 2007)

Historically, this mechanism of polymerization is divided into the following steps; initiation, propagation, and termination.

2.3.1 Initiation

Initiation is the first step of the polymerization process. In this stage, an active core is formed from which a polymer chain is generated. Radical initiation works best on monomers that have carbon-carbon double bonds and carbon-oxygen double bonds. Initiation has two steps; 1) one or two radicals are created from initiating molecules, and 2) radicals are transferred from initiator molecules to available monomer units. The most notable initiation methods are as follow:

Thermal decomposition: Initiator molecules are heated and a bond is branched, producing two radicals.

Photolysis: Radiation cleaves a double bond homolytically and forms two radicals.

Redox reactions: The reduction of hydrogen peroxide or an alkyl hydrogen peroxide by iron can make active free-radicals.

Persulfates: Persulfate dissociates in the aqueous phase.

Ionizing radiation: α-, β-, γ-, or x-rays cause discharge of an electron from initiating species. Another molecule will capture that electron to produce a radical.

Electrochemical: Electrolysis of a solution containing both monomer and electrolyte. Radical anion and cation are formed when the monomer molecule receives an electron at the

cathode, and the monomer molecule will donate an electron at the anode. The radical ions can initiate free radical polymerization.

Plasma: A gaseous monomer is placed in an electric discharge under low pressure conditions. (The conditions that a plasma (ionized gaseous molecules) is created). In most cases, the system is heated and/or placed in a radiofrequency field.

Sonication: High-intensity ultrasound at high frequencies (higher than 16 kHz) can be applied to a monomer. Initiation results from the effects of cavitation (the formation and collapse of cavities in a liquid). The collapse of these cavities generates high local temperatures and pressures.

Due to side reactions and inefficient synthesis of the radical species, the efficiency of chain initiation is not 100%. The efficiency factor, f, is used to define the effective radical concentration(Hageman 1985, 123-150).

2.3.2 Propagation

During polymerization, an active polymer chain spends most of its time in increasing its length, or propagating. After the radical initiator is formed, it attacks a monomer most likely in the monomer's more loosely held bond (in its a pi bond). The free radical utilizes one electron from the pi bond to form a stable bond with the carbon atom. The other electron returns to the second carbon atom, which results in the formation of another radical. After a chain starts to propagate, it reacts with the available monomers until there is no more unreacted monomer or until termination occurs(Georges and Kazmeier 1993, 5316).

2.3.3 Termination

Termination reactions are mainly:

1. Combination of an active chain end with an initiator radical.

2. Interaction with impurities or inhibitors. Oxygen is the common inhibitor. The growing chain will react with molecular oxygen, producing an oxygen radical, which is much less reactive.

By controlling the termination reactions of a free radical polymerization, the degree of polymerization and average molecular weight of a polymer can be influenced.

In chapter 5, Modeling and Simulation, we will demonstrate the reaction mechanisms that are considered to govern the polymerization reactions in our setup.

2.4 Microparticles synthesis methods

Hydrogel microparticles are polymeric particles between 0.1 and 100 µm in size. They can be produced using a wide range of methods. These synthesis methods are divided into two main groups, namely, bottom up (bulks methods) and top-down (direct methods). Our focus in this thesis are mainly on top-down methods; however, a brief introduction to bottom-up methods, their main features and typical applications are addressed in **Chapter 2.3**.

2.4.1 Bottom-Up (Bulk) Synthesis of Microparticles

Bottom-up approaches refer to bulk methods that traditionally use emulsification to form tiny droplets and polymerizes them using radiation or heat. The particle size distribution varies based on the reaction and kinetic parameters such as temperature and pressure.

Bulk emulisification methods can produce a large quantity of particles in a relatively controllable environment. Due to the cost-efficacy, most applications of microparticles such as in

cosmetics, templates for nanoparticle synthesis(Sooklal et al. 1998, 1083-1087), photonic crystals(Xu et al. 2003, 468-472), microgel lenses(Shogenji et al. 2004, 1355-1359), and targeted drug delivery(LaVan, Lynn, and Langer 2002, 77-84) still consist of microparticles prepared by these methods(Das, Zhang, and Kumacheva 2006, 117-142).

Bulk emulsification microparticle synthesis methods have mostly been limited to the production of spherical or spheroidal particles. Although these approaches are feasible to produce many particles at a low cost, they fail to accommodate the increasing demand of structural complexity. Shape control, beyond spheres, is extremely difficult with bottom-up approaches for both polymer and composite microparticles. Bulk emulsification methods also fail to generate particles with non-uniform chemistries. As a result, these techniques are ill-suited for growing requests that demand high degrees of both chemical and mechanical complexity(Helgeson, Chapin, and Doyle 2011, 106-117).

2.4.2 Top – Down Methods

2.4.2.1 Direct Methods

Direct methods are microparticle fabrication techniques that utilize point-by-point or layer-by-layer radiation of a laser beam. A well-studied sub-group of the direct methods for synthesizing 3D structures is multiphoton fabrication which provides the control of morphology in all dimensions. The basic requirement for the multiphoton fabrication is that an absorption event is caused by the combined interference of two or more photons, all of which must be present at the same time to provide enough energy to initiate a reaction(Kaiser and Garrett 1961, 229-231). Complex structures can be fabricated by moving the laser focus in three dimensions relative to the substrate. The multiphoton fabrication enables the synthesis of complex, 3D particles with high-resolution feature sizes as small as 100 nm(LaFratta et al. 2007, 6238-6258).

On the other hand, multiphoton fabrication, like other direct methods, is relatively expensive and time-consuming, and is not suitable for applications that require many particles. However, this method accomplishes to make high resolution complex structures that are not attainable from other methods(Bong, Pregibon, and Doyle 2009, 863-866).

The main drawbacks of the direct methods are

- Limitation of materials used: most of the materials that are typically polymerized with direct laser beam used in these methods are not biocompatible.
- Limitation of efficiency: the direct fabrication methods are time-consuming processes. Multiphoton-fabricated microparticles are often too expensive to be utilized in applications that require large numbers of particles.

As a variation of the multiphoton fabrication, Femtosecond laser direct writing (FsLDW) has been established as a nano-enabler that can produce high-resolution complex particles. FsLDW is able to synthesize three-dimensional shapes, with a high fabricating resolution up to tens of nanometers which is far beyond the optical diffraction limit of polymerizing light. However, its shortcoming for industrial use is also apparent, i.e., the relatively low fabrication efficiency caused by the nature of single beam scanning(Zhang et al. 2010, 435-448; - Sugioka and - Cheng , - 3576).

2.4.2.2 Lithographic based methods

Patterned hydrogel microparticles can be prepared by litghographic-based methods as shown in **Figure 2-3**. Predominantly, the lithographic processes use photoinitiated free radical polymerization due to controlled initiation and relatively fast propagation kinetics compared to other types of polymerization. In this case, the photo-curable precursor solution at minimum

consists of a photoinitiator, a crosslinker agent, and monomer(or oligomer) solution (Dubinsky et al. 2008, 3555-3561).

Photolithography, is a microfabrication process to pattern parts of a thin film or the bulk of a substrate. It uses light to transfer a geometric pattern from a photomask to a light-sensitive chemical "photoresist" on the substrate. Photolithography can engineer particle properties and leads to the production of homogenous ensembles of particles. Therefore photolithography-based methods significantly expanded the design of microparticles, enabling their use in modern applications such as in self-assembled and stimuli-responsive materials, and micromechanical systems. Moreover, since the lithographic production of hydrogel colloids occurs as a single-step synthesis, molecular and colloidal objects can be simply encapsulated into the resulting hydrogel particles (Helgeson, Chapin, and Doyle 2011, 106-117). On the other hand, the batch nature of the process leads to a low particle throughput and therefore limits its applications in industry. Moreover, producing chemically anisotropic particles using photolithography requires multi-step projection of polymerizing light which is hard to achieve in a high-throughput fashion(Dendukuri et al. 2007, 818-828).

Soft lithography refers to a group of techniques for producing structures using "elastomeric stamps, molds, and conformable photomasks". Since elastomeric materials (Polydimethylsiloxane (PDMS) for example) are used in this method, it is called "soft"(Rockett. 2012, 45). Soft lithography is capable of constructing features measured on the micrometer to nanometer scale.
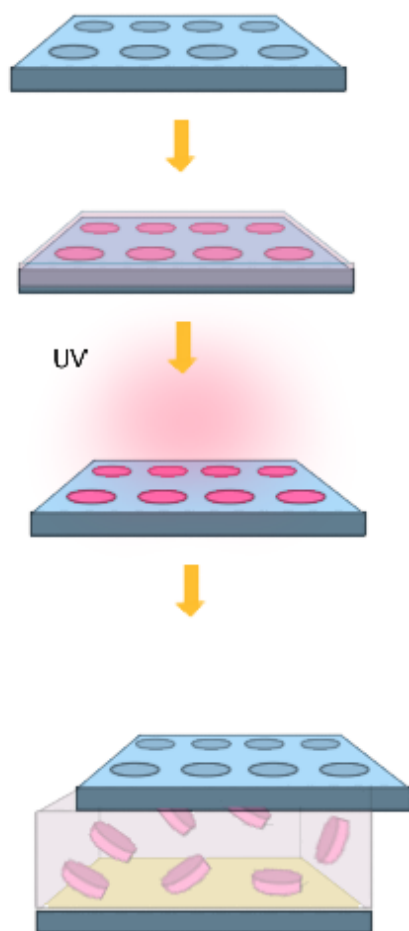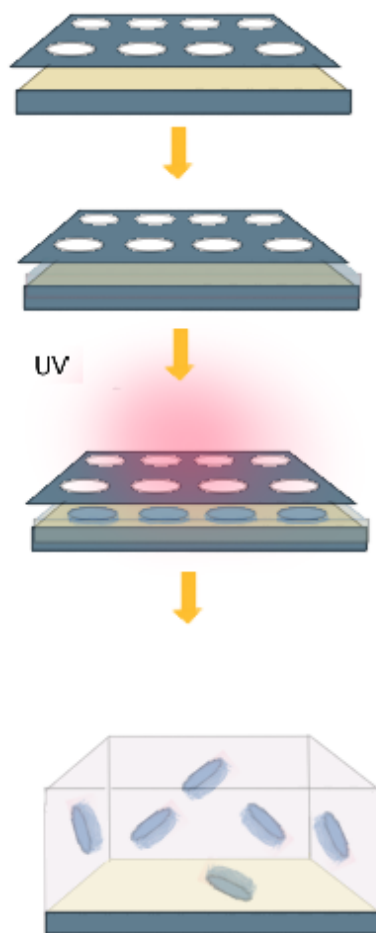
Figure 2-3 Lithographic based methods for synthesizing 2-dimensional microparticles; left) Imprint lithography method; right) photolithography method

2.4.2.3 PRINT Method

Particle replication in a non-wetting template (PRINT) is a multistep microfabrication technique for making a large number of particles (**Figure 2-4**). The PRINT process for fabricating isolated particles starts with an etched silicon master created using soft-lithographic techniques.

Then the photo-curable liquid PFPE resin is poured on to the silicon master and permitted to distribute evenly by gravitational force across and wet the surface of the master template. The resin is then photochemically crosslinked to form a strong elastomeric Perfluoropolyether (PFPE) mold that is subsequently peeled away from the master to reveal micro- or nanoscale holes on its surface. Next, a precursor solution is cast on a high surface energy sheet, typically poly(ethylene terephthalate) (PET), to form a uniform film of quantified thickness. The sheet is then laminated to the empty PFPE mold using heat and pressure. When the covering sheet is peeled away, capillary forces keep the liquid trapped in the mold. The pre-particle solution in the filled mold cavities is then solidified using an appropriate means (UV light, thermal heating, etc.). Lastly, the solidified particles in the mold are removed by laminating the filled mold to a sacrificial harvesting film such as polyvinylpyrrolidinone, poly(vinyl alcohol) or cyanoacrylate. Peeling the film apart from the mold outcomes in an array of particles on the harvesting sheet. Free particles can then be collected by dissolving away the sacrificial adhesive film with an appropriate solvent for the adhesive and a non-solvent for the particles(Xu et al. 2013, 6580-6589).

Unfortunately, the complexity of hydrogel particles synthesized by the PRINT method is constrained by practical limitations in the production of template molds. Bending and buckling of the lithographic template limit the transfer of patterns with high-aspect ratios or internal features. Moreover, materials used for this method should be carefully chosen, because the mold should remain non-wetting to the precursor. Moreover, the chemical anisotropy of produced particles is limited to striped particles (Bong, Pregibon, and Doyle 2009, 863-866).

Figure 2-4 Print Method

2.4.3 Microfluidics-Based Methods

Microfluidics has emerged as a powerful tool for chemical and biological manipulations and assays. Low Reynolds number allows the manipulation of flow in an extremely controllably fashion. Benefits of microfluidics include reduced reagent consumption and analysis time, as well as the ability to integrate multiple functions onto a single device.

The typical size of microfluidic channels range from a few micrometers to some hundred micrometers and the typical flow velocities stay below 10 mm/s resulting in Reynolds numbers well below 100 for water(Seemann et al. 2012b, 016601). Since most microfluidic experiments are

performed at laminar flow conditions, mixing proceeds dominantly by molecular diffusion which is rather slow at typical microfluidic channel widths.

Microfluidic systems for microparticle synthesis divide into two important categories. In **droplet-**based (''digital'') microfluidic devices, a liquid is transported in the form of droplets on a planar array or between two parallel plates, rather than as a stream in a channel. In **Flow lithography-**based methods, fluids are manipulated as continuous flow in micron-dimension channels(Reyes et al. 2002, 2623-2636).

2.4.3.1 Droplet-Based Microfluidic

In droplet-based microfabrication, a large number of extremely monodispersed droplets of a desired polymer precursor are first produced using either a T-junction(Xu et al. 2006, 3005-3010) or flow-focusing(Takeuchi et al. 2005, 1067-1072) geometries in a microfluidic device (**Figure 2-5**). The droplets are then solidified using light or thermal polymerization to produce monodispersed polymeric particles. The precise control of droplet volumes and reliable manipulation of individual droplets such as mixing of their contents allows researchers to perform chemical reactions within the droplets under well-defined conditions(Seemann et al. 2012a, 016601).

The integration of a flow-focusing configuration or T-junction geometry into a microchannel fabricated using soft lithography allows the controllabe manipulation of droplet size. The operating diagram of droplet size as a function of flow rate and flow rate ratios illustrates regimes with both monodisperse and polydisperse droplets.

By confining droplets using the channel dimensions and geometry of a microfluidic device and by using coflowing laminar streams, polymeric plug, disk, hemisphere, core-shell and Janus particles can be synthesized. However, these techniques are restricted to producing shapes that are either spherical or deformations of spheres(Dendukuri et al. 2007, 818-828).
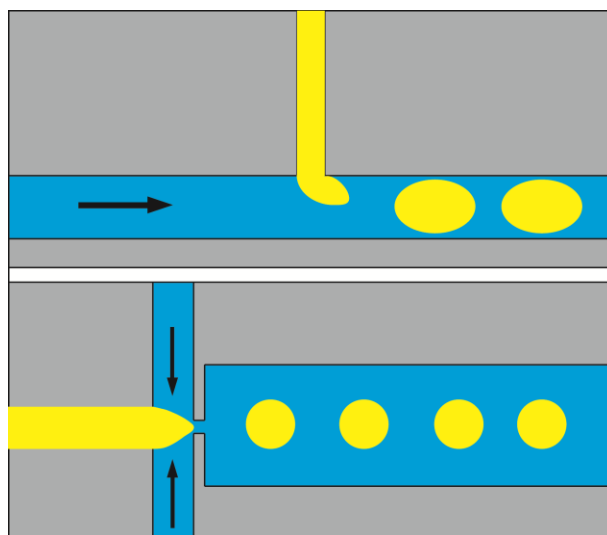
Figure 2-5 Droplet-based microfluidic particle synthesis; top) T-junction channel geometry; bottom) flow-focussing channel geometry. The black arrow shows continuous phase flow direction

2.4.3.2   Flow Lithography

The ideal process for microparticle synthesis would be able to produce highly homogenous particles with well-defined shape or chemical anisotropy. Moreover, it would be versatile enough to accommodate different materials. Finally, the process would be scalable to amounts of commercial interest by remaining cost-effective(Helgeson, Chapin, and Doyle 2011, 106-117).

The combination of a photolithographic technique with microfluidics and led to the invention of **Flow-Lithography** methods. Thus, flow-lithography, has the advantage of performing the particle patterning process in a continuous fashion.

In the simplest form of a flow-lithography setup known as Continuous-Flow Lithography (**CFL**), a load of precursor containing a photosensitive initiator is passed through a rectangular, PDMS microchannel device. Particle arrays of photomask-defined shape are synthesized by exposing the flowing oligomer to controlled pulses of ultraviolet (UV) light using an inverted microscope and collected in the device reservoir. Rapid polymerization kinetics permits particle formation quickly (<0.1 s), and the oxygen-aided inhibition layers near the PDMS surfaces allows resulting particles to flow without sticking to the PDMS walls (as illustrated in **Figure 4-1a**) (Decker and Jenkins 1985, 1241-1244) .

The shape of synthesized particles in the x–y plane is determined by the shape of features used on the transparency mask, while the particle thickness is dependent on the height of the channel used and the thickness of the oxygen inhibition layer. The particle shape is extruded throughout the channel height. This allows the fabrication of almost any two dimensional shape. But the fabrication of non-spherical 3D dimensional particles remains challenging.

Flow-lithography improves particle synthesis in several aspects. It does not require complex three-dimensional channels for creating non-spherical particles. Moreover, multi-step washing and cleaning the channel is not needed, as the flow itself washes the synthesized particles and also loads uncrosslinked precursor to the reaction zone. Co-flow laminar streams of two or more individual polymer pre-cursors, can lead to the creation of Janus particles that exhibit chemical anisotropy. Flow lithography is a one-step, cost-effective, high-throuput method to create a large number of monodispersed particles and it can be multiplexed as needed.

Stop-flow lithography (**SFL**) (as shown in **Figure 2-6**) is an improved version of CFL where a precursor stream is connected to a computer controlled pressure valve that switches between on (flow) and off (stop) in desired time steps. Before the exposure of UV starts, flow

stops, so 2D shaped extruded particles can be synthesized in an immobile environment. This results in a higher particle resolution and sharper interface compared to CFL. Just after the particles are synthesized, they are flushed out to the reservoir and a new stream of precursor is introduced to the reaction zone(Dendukuri et al. 2007, 818-828).
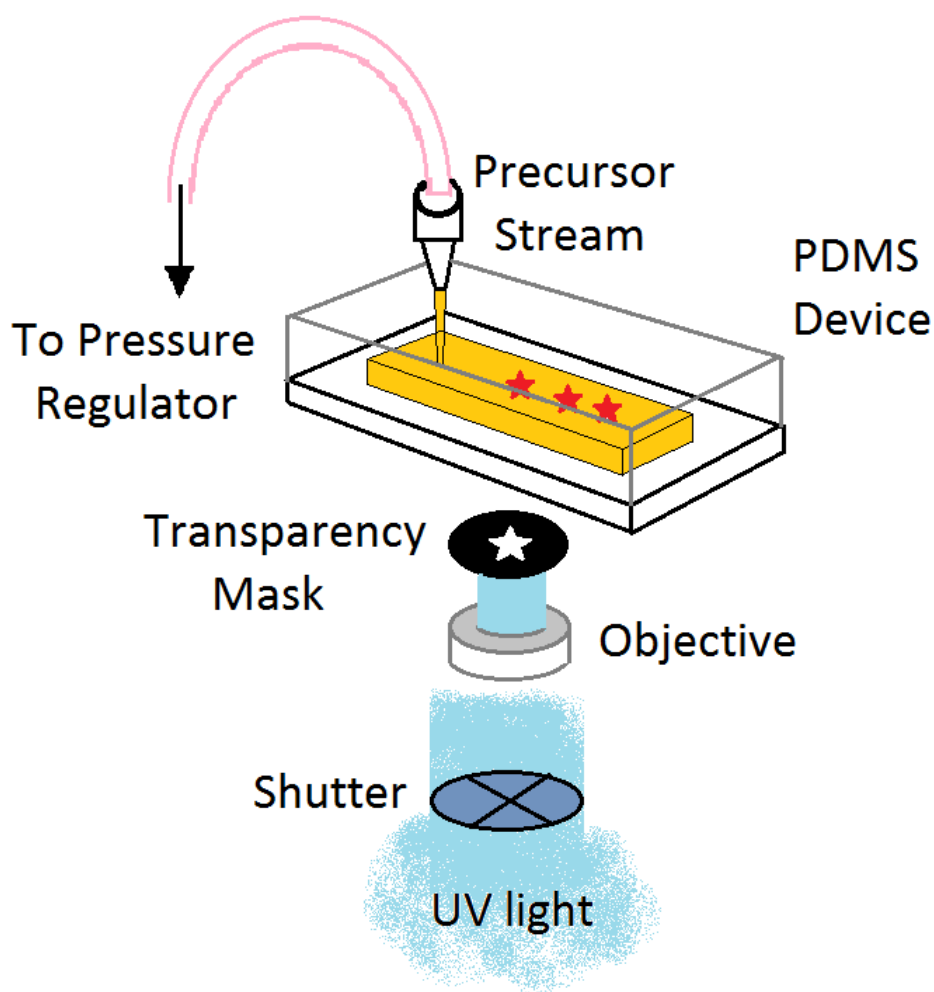
Figure 2-6 Stop-Flow Lithography

Similar to other photolithographic-based methods, the particle shape in the x-y axis is defined by a photomask . These photomasks can be replaced by dynamic micromirror device

(DMD) for real-time particle shape definition. This combination of the programable optical projection and microfluidic devices allows one to precisely control the timing and location of photopolymerization process for microstructure fabrication(Lee et al. 2009, 1670-1675; Chung et al. 2007).

In flow-lithography techniques, particles can be transported and manipulated downstream under moderate laminar flow conditions, allowing for facile further processing in situ after synthesis, such as purification, functionalization, or assembly.(Kanazaki and Okada 2012, 10750-10755)

As an upgrade to SFL, Lock Release Lithography (LRL) utilizes a combination of channel topography, mask design, and pressure-induced channel deformation to form and release particles in a cycled fashion. 3D particles can be made from this technique, but the cost of particle synthesis increases due to the requirement of complex 3D microchannels.

The number of flow-lithography techniques being proposed for the synthesis of 3D particles, namely, stop-flow interface lithography(Jang et al. 2007, 9027-9031), lock release lithography (**LRL**)(Bong, Pregibon, and Doyle 2009, 863-866), soft membrane deformation and optofluidic maskless lithography(Lee, Yoon, and Lahann 2011, 195-202; Lee et al. 2009, 1670-1675), tuning particle curvature using a tuning fluid(Panda et al. 2009, 5986-5992), and three-dimensional fluidic self-assembly by axis translation of two-dimensionally fabricated microcomponents(Chung, Jung, and Kwon 2011, 796-803), suggest that a simple flow-lithography method for making complex 3D particles is highly desirable. Yet, all of the existing methods produce particles with limited 3D features, and often require difficult-to-manufacture 3D channels. To date, single-step synthesis of truly 3D particles from a simple 2D microfluidic channel has remained difficult to accomplish.

Table 2-1 compares the advantages and disadvantages of different particle synthesis method in terms of **monodisparity**, **chemical complexity**, **biocompatibility**, **cost efficiency**, and **shape complexity.**

Table 2-1 Microparticle synthesis methods comparison

	Monodisparity	Chemical complexity	Biocompatibility	Cost Efficiency	Shape Complexity
Bulk		*	*	*	
Direct	*				*
PRINT			*	*	
Droplet microfluidic	*	*	*	*	
SFL	*	*	*	*	
LRL	*	*	*		*

2.5 Conclusions

3D particles have remained difficult to synthesize. Particles with high curvature are expensive and time-consuming to synthesis using direct methods and not attainable using bulk or PRINT methods. Thus the requests from applications that require lots of complex particles have not been properly addressed. Because lack of cheap intricate microparticles, their behavior and potential applications have not been properly studied.

Stop-flow lithography has shown its liability in making uniform 2D particles in mass numbers. It significantly reduces the cost of microparticle synthesis compared to direct methods.

The number of flow-lithography techniques being proposed for the synthesize of 3D particles, namely, stop-flow interface lithography(Jang et al. 2007, 9027-9031), lock release lithography(Bong, Pregibon, and Doyle 2009, 863-866), soft membrane deformation and optofluidic maskless lithography(Lee et al. 2009, 1670-1675), tuning particle curvature using a tuning fluid(Panda et al. 2009, 5986-5992), and three-dimensional fluidic self-assembly by axis translation of two-dimensionally fabricated microcomponents(Chung, Jung, and Kwon 2011, 796-803), suggest that a simple flow-lithography method for making complex 3D particles is highly desirable. Yet, all of the existing methods produce particles with limited 3D features, and often require difficult-to-manufacture 3D channels. To date, single-step synthesis of truly 3D particles from a simple 2D microfluidic channel has not been implemented.

In this thesis, we develop a flow-lithography based-method that has the ability to generate complex 3D functional particles in a 2D channel.

CHAPTER 3

MATERIALS AND METHODS

3.1 Microfluidic device fabrication

Microfluidic devices used in this research is produced by replica molding using poly(dimethylsiloxane) (PDMS). We used the commercially available kit 'Sylgard 184' from Dow Corning that consists of a base and an agent mixed in a mass ratio of 10:1. In this section the basic principle of the microfabrication methods using soft lithography is explained for PDMS devices. To fabricate PDMS devices, typically a master is produced by standard contact photolithography and a replica is generated from this master by pouring the pre-mixed PDMS-kit and heat curing.

3.1.1 Masters (Molds)

We used photolithography to form a mold for casting the PDMS structure with a laser printed mask and light source to pattern a photosensitive resist polymer to match the features of the mask.

We chose SU-8 2000 (MicroChem, Newton MA USA) for making the mold for casting the PDMS. We spin coated SU-8 polymer photoresist as poured onto a Si wafer substrate. The channel height is determined by the speed of spin coating. We prebaked the SU-8 coated wafer at 90 °C on a polished Al hot plate for 75 min. Then the wafer was covered with the mask and mounted to be exposed with UV radiation with a wavelength of 350–400 nm.

After patterning the silicon mold, the positive channel features were developed. Then the mold was immersed in MicroChem's SU-8 developer and then post baked for 2h at 90°C.

3.1.2 Casting the microchannels

The casting process is simply placing the mold in a heat-tolerant plastic tray and pouring PDMS onto the mold. Then the result is placed in an oven at 65 °C for 2 h for curing the PDMS. Then we peel off the baked PDMS from its mold and cut as desired.

After cutting off the PDMS from the master, channels are cut individually. Then we pierce the inlet and outlet for each channel. The outlet is usually bigger and act as a reservoir for collecting synthesized particles. Then the PDMS channels are washed using ethanol to remove any impurities and non-polymerized PDMS from the channel. We float the PDMS channels in tiny tubes filled with ethanol, and sonicate for at least 10 mins. The PDMS channels are then taken out of the ethanol tube, and dried using a nitrogen high pressure capsule.

We attach the PDMS channels on a partially cured PDMS layered glass substrate. The PDMS layered glass slides are prepared by pouring a small amount of PDMS on the glass, and spread it evenly on the glass. Then the glass slides are partially cured for 25 mins at 65 °C. The PDMS channels are then mounted on the glass slides to complete the microchannel. Then we baked the microchannel for another 2 h in order to let the channel bond to its substrate. **Figure 3-1** shows an example of PDMS microchannels mounted on PDMS layered glass substrates.
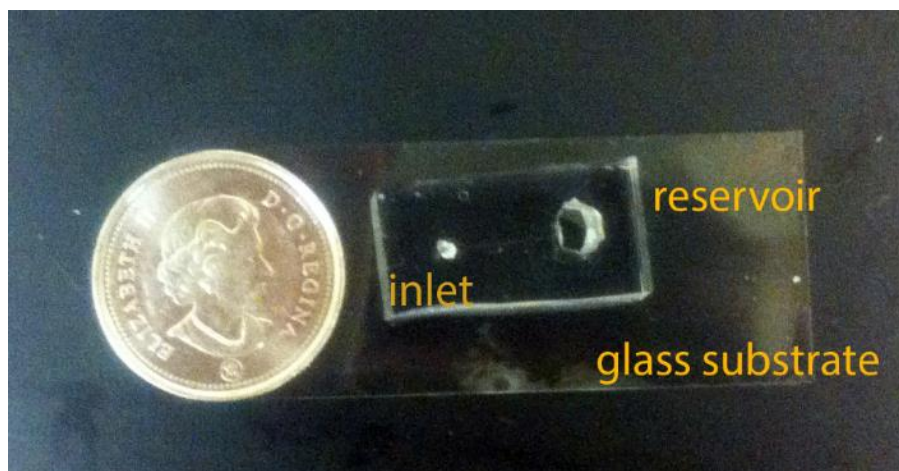
Figure 3-1 PDMS microchannel assembled to a PDMS coated glass substrate.

Figure 3-2 shows a simple PDMS channel photomask design that is used to generate

microparticles in our experiments. We used a PDMS microchannel with 500 ± 10 µm width and

…   height.
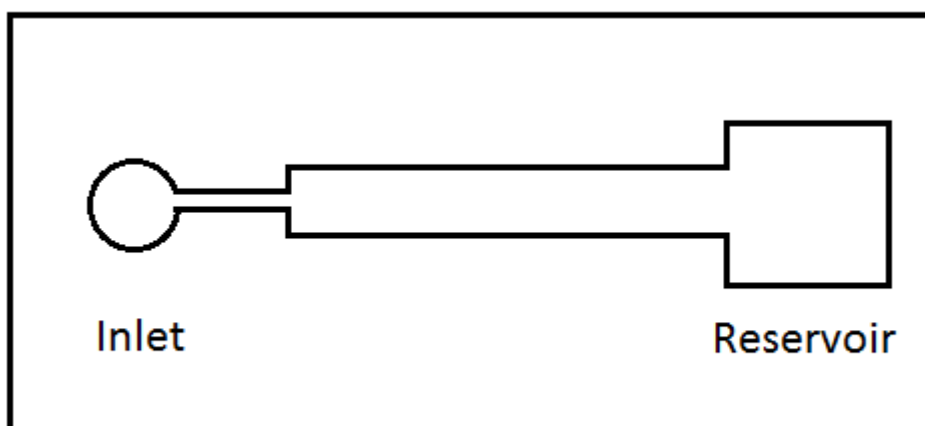
Figure 3-2 Simple PDMS photomask microchannel design

We assembled pipet tips (ART 10 Reach and ART 200, molecular BioProducts, Inc.) to the

inlet of the channel to flow our precursor solutions in the channel. The channels were mounted

on an inverted microscope (Axiovert Observer .A1, Zeiss) for particle synthesis.

3.2 Materials

Magnetic polymeric microparticles are synthesized from a precursor solution prepared by mixing 35% (v/v) poly(ethylene glycol) (700) diacrylate (PEG-DA 700, Sigma-Aldrich), 5% (v/v) 2-hydroxy-2-methylpropiophenon (Darcour 1173, Sigma-Aldrich) initiator, 20% (v/v) water-based ferrofluid (EMG 508, Ferrotec), and 40% (v/v) water. Non-magnetic particles are prepared using 35% (v/v) PEG-DA 700, 5% (v/v) Darcour 1173, and 60% (v/v) water. Following synthesis, we collected the particles from a reservoir at the downstream of the PDMS channel and washed them several times with 0.5% (v/v) Tween-20 (Sigma Aldrich) solution in water.

We made hydrogels from PEG-DA (**Figure 3-3**) which is a synthetic, hydrophilic crosslinking material which forms polymers in the presence of photoinitiator and UV light. PEGDA is widely recognized as a biocompatible and non-immunogenic.
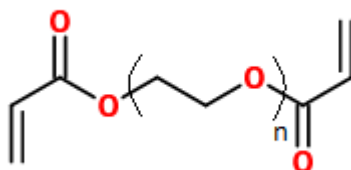
Figure 3-3 Polyethylene glycol diacrylate (PEG-DA) molecular structure

Here we used a solution of Tween-20 (**Figure 3-4**) in water to prevent particle loss because of sticking to the pipet tips and tubes.
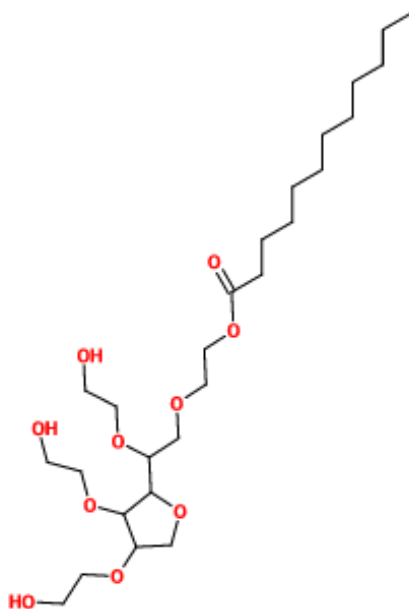
Figure 3-4 Polyoxyethylene (20) sorbitan monolaurate (Tween-20) molecular structure

3.3 Photopolymerization Setup

We synthesized our particles in a stop-flow lithography based setup (**Figure 3-5**, **Figure 3-6**). The particles were photopolymerized when the flow is stopped. Then synthesized particles are pushed out of the photopolymerization area by resuming the flow of fresh precursor solution and this cycle repeats. A command script governed a pressure valve (Type 100LR, ControlAir Inc.) to switch between on (allowing a 2 psi air pressure to induce the flow in the channel) and off (unpressurized). The script also governed a digital UV shutter (Lambda SC, Sutter Instruments) that was switching between on and off, on the way of UV illumination from our UV source (Lumen 200, Prior Scientific, Inc.). We used a UV filter (11000v2, Chroma) to select UV light at desired wavelength for polymerization. Transparency masks (CAD/Art Services, Inc) were designed with AUTOCAD 2011 and placed at the field-stop of the microscope to shape the UV light. A 20x objective (20x/0.4 korr LD Plan-Neofluar, Zeiss) was used to make a cylindrical UV exposure path throughout the channel height to make the bullet shaped particles (**Figure 4-2**), and

a 40x objective (40x/0.6 korr LD Plan-Neofluar, Zeiss) was used to shape the UV light to have a higher incident angle to make particles shown in chapter 4.2. For tuning the focal point of UV light at desired heights of the channel, we first focus the objective at the bottom of the channel so as the clearest image of the glass substrate was achieved. Then the objective-to-stage distance was adjusted by the microscope focus drive to achieve the desired relative focus plane position, knowing that in our microscope, each line of the focus drive represents 2 μm displacement of the microscope stage height. A Nikon D300s camera (DigitalSLR) was used to capture bright field images of the synthesized particles. Finally, we used scanning electron microscopy (FE-SEM S-4500, Hitachi) to capture their SEM images.
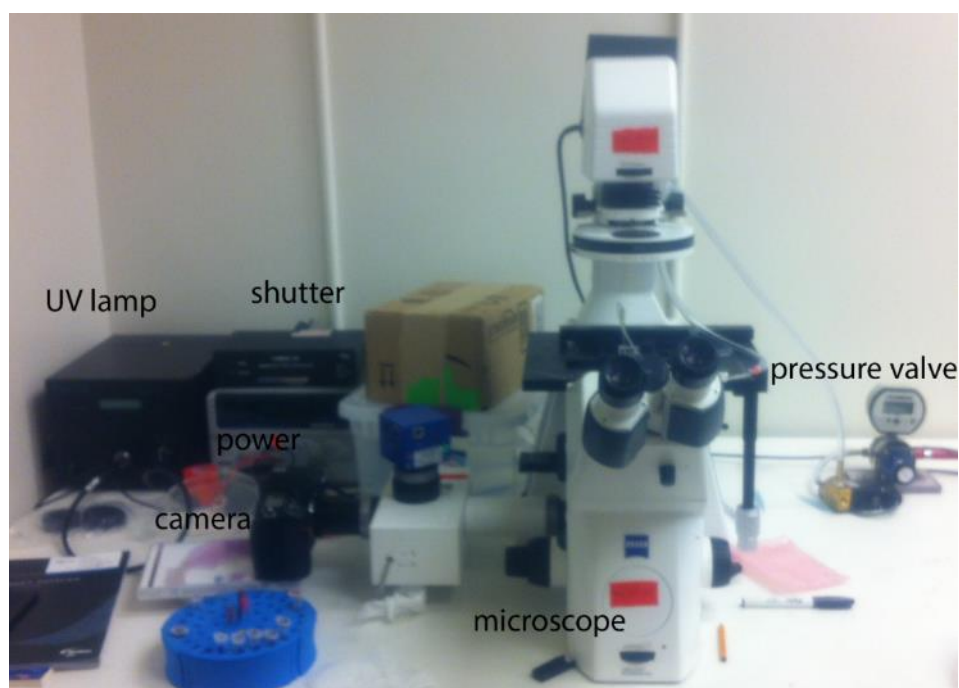
Figure 3-5 Stop-flow lithography setup that we used for particle synthesis
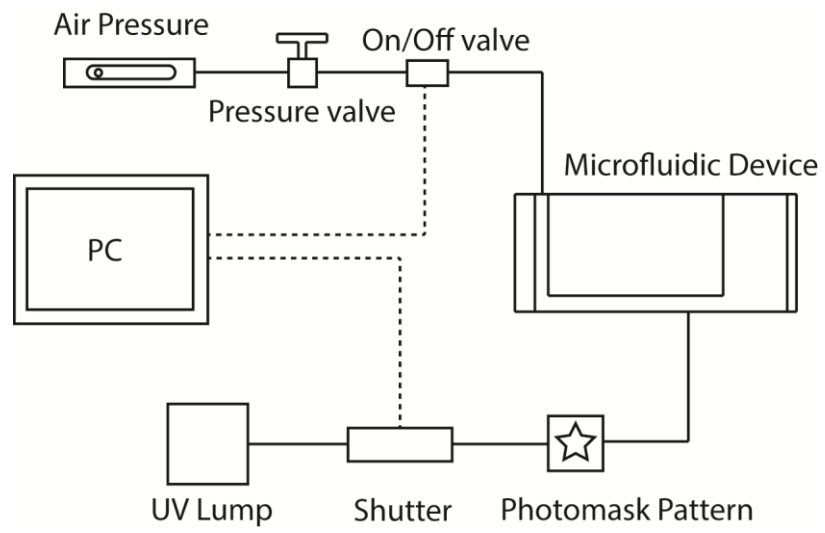
Figure 3-6 Stop-flow lithography setup schematic

CHAPTER 4

EXPERIMENTAL RESULTS

In this chapter, we describe our method and illustrate different mechanisms that create microparticles with 3D curvature and branched structures in our setup.

Our method exploits the non-uniformity of the polymerizing ultraviolet (UV) light, UV absorption by opaque nanoparticles in the precursor solution, and uses discontinuous photomask patterns, to make highly curved 3D microparticles. We investigate the microparticle shape dependence on each parameter by independently tuning the field and focus of the UV light, adding opaque magnetic nanoparticles to the precursor solution, and using a variety of photomask patterns.

4.1 The Effect of Precursor Solution Opacity

Figure 4-1 is a schematic diagram of our setup for producing 3D particles. We synthesize hydrogel particles using a stop-flow lithography-based method, where a solution of monomer, photoinitiator, and hydrophilic ferrofluids flow in a microchannel, and is polymerized by projection of a UV light through a photomask (See **Section 3.3** photopolymerization setup for details). **Figure 4-1**b is a cross-sectional view of polymerization area that is used to create bullet-shaped particles. While previous microfluidic flow lithography techniques have tried to avoid having non-uniform UV light along the exposure path, in this setup we use opaque magnetic nano-particles in our hydrogel precursor to generate a gradient of the incoming UV light along the channel height, to create functional particles with parabolic curvature in a one-step fashion.
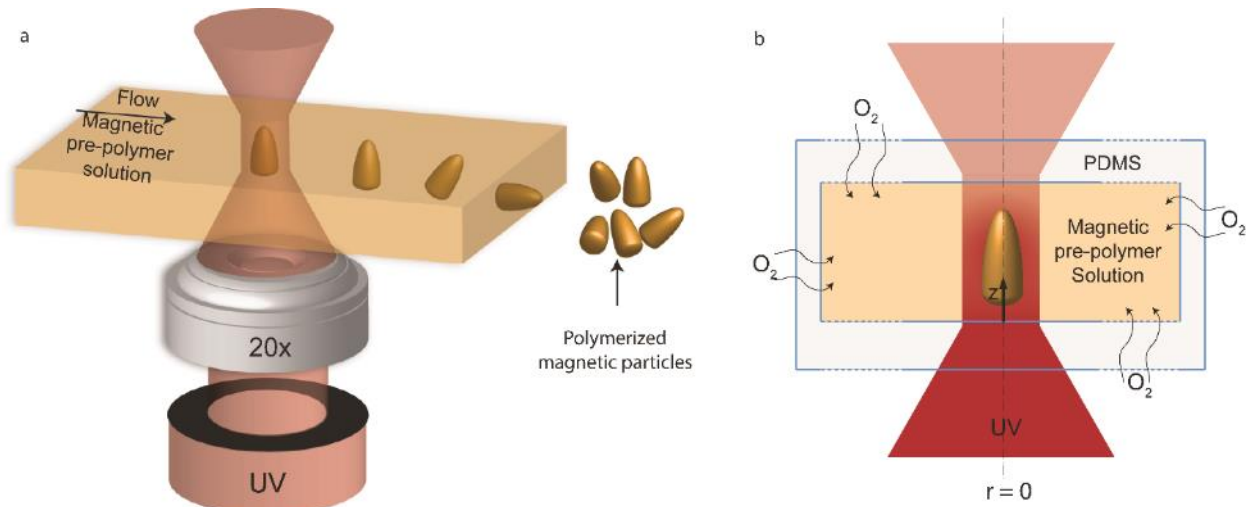
Figure 4-1 Schematic diagram of our particle-synthesis method and experimental images of bullet-shape magnetic microparticles. **a)** A magnetic precursor solution including monomer, photoinitiator, and hydrophilic ferrofluids flow in the microchannel, and is polymerized by the UV light. Polymerized magnetic particles are manufactured in a conveyer-belt fashion, where the flow stops in fixed time increments and the UV light polymerizes the solution. **b)** A cross-sectional schematic view of our particle synthesis technique. The UV light gradient in z direction is primarily produced by opaque nanoparticles in the solution. The amount of polymerization that takes place is controlled by the local UV light intensity and oxygen concentration. The curved shape of the particle results from a combined effect of the UV light gradient and the oxygen concentration gradient.

A row of bullet-shaped curved 3D particles is shown in **Figure 4-2**. These particles are synthesized upstream of the image recording region using a simple 2D circle photomask (**inset of Figure 4-2**), in a PDMS channel with height, $H = 40$ μm. The depth of focus of the UV light, $T_{focus,}$ $= 51$ μm, and we use a 20x objective with numerical aperture, N. A. $= 0.4$. We expect a straight cylindrical UV light path through the thickness of the channel, because the depth of focus is larger than the channel height (See Chapter 5.2.1 for more details). Here, the incoming UV light is not uniform in the radial direction even when the light is focused. After propagating through the photomask hole and the objective lenses, the diffracted light is more intense at the center of its propagation path and its intensity diminishes away from the center. (See Chapter 5.2.2 for more details)
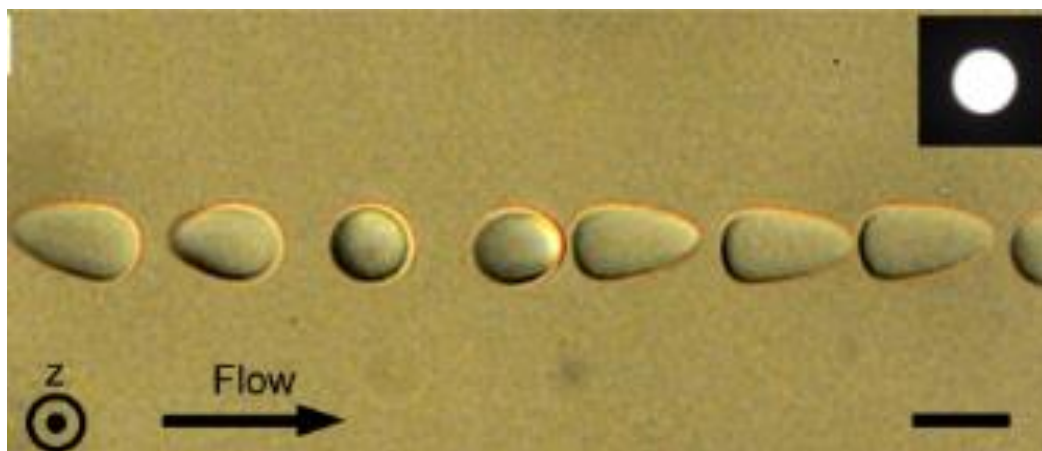
Figure 4-2 A row of freshly formed bullet-shaped magnetic particles synthesized in a 2D 40 μm tall microchannel. Here we use a 20x objective (N. A. = 0.4, T_{focus} = 51 μm) to produce a cylindrical UV light path across the channel height. The inset is a picture of the photomask we use. Scale bar 20 μm.

The inclusion of opaque magnetic nano-particles in the monomer mixture affects the penetration of the incident UV radiation by absorbing the UV light. Thus, the UV light intensity diminishes along the channel height. Since the photolysis rate of the initiator, which produces free-radicals, is proportional to the local light intensity, the UV light attenuation leads to a free-radical concentration gradient along the channel height and also in the radial direction. These free-radicals, which can start and carry on the polymerization reactions, are also inhibited by the dissolved oxygen present in the precursor solution. Molecular oxygen prevents the polymerization by reacting with initiator, primary, and polymer radicals to form peroxy radicals.(Decker and Jenkins 1985, 1241-1244) Since the peroxy radicals do not facilitate polymerization, the oxygen molecules are essentially scavenging and terminating free radicals. Some of the oxygen consumed in these reactions is replenished by oxygen continually diffusing in through the PDMS walls. This competition between reaction and diffusion of oxygen, ensures that there is an uncrosslinked "lubrication layer" close to the PDMS channel walls.(Dendukuri et al. 2008, 8547-8556)

This reaction-diffusion process combined with the non-uniformity (radial and axial) of light intensity produces a gradient of effective free-radical concentration, ranging from a maximum near the bottom center of the channel cross section, to a minimum at the channel walls. As a result, the synthesized magnetic particles have nearly flat bottoms, and curved profiles on the far side of the light source along the channel height (**Figure 4-2**), rather than the symmetric rod shapes typically observed in the absence of absorbing additives.(Jang et al. 2007, 9027-9031) At lower parts of the channel height, the incoming UV light produces free-radicals at a sufficiently high rate to offset the effect of oxidation reactions. Thus, in lower regions closer to the UV light source, there are more polymerization reactions, compared to the higher regions of the channel, where the weakened UV light only initiates sufficient polymerization reactions in the inner parts of the light path. In the upper region, precursor close to the center of the light path polymerizes beyond the gelation point, while almost the entire precursor in the lower region of the light path solidifies into a gel. Thus, particles with curved walls are synthesized, and the curvature is enhanced by the radial gradient of the incoming UV light, in the presence of the UV absorbing additive.

Figure 4-3 shows rod shaped particles synthesized from a prepolymer solution without magnetic nanoparticles. . The symmetrical, rod shape of these particles suggest that the light absorbance in the absence of magnetic nanoparticles in the precursor solution is insignificant.
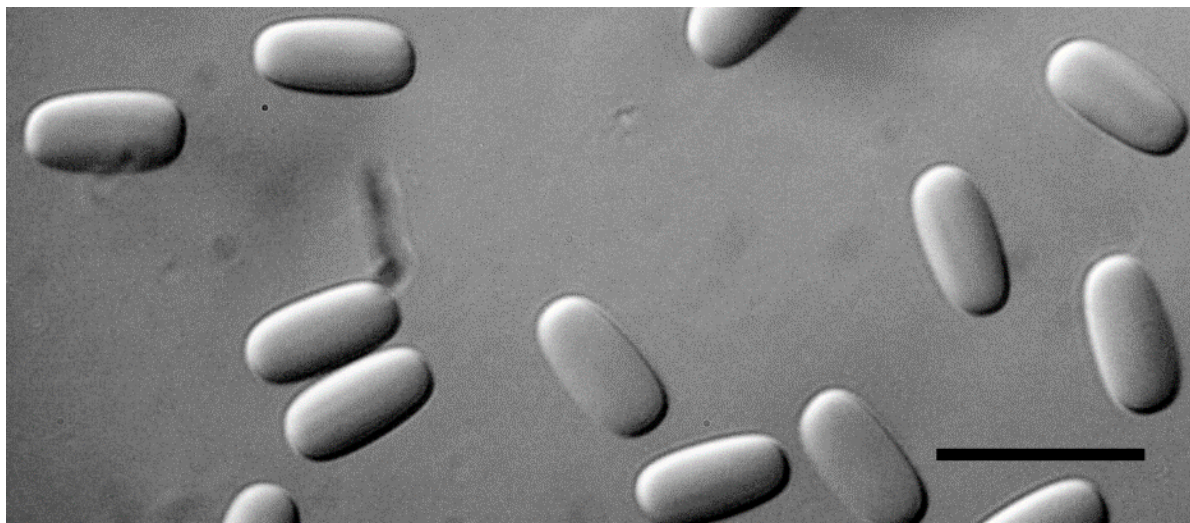
Figure 4-3 Hydrogel particles synthesised from a monomer and photoinitiator solution. Scale bar 50 µm

4.2 The Effect Out of Focus Polymerization

We are also able to synthesize 3D shaped particles in our 2D microfluidic system, without including opaque materials in our precursor solution (**Figure 4-4** and **Figure 4-5**). We use a high numerical aperture 40x objective (N. A. = 0.60, T_{focus} = 18.5 µm), with H = 300 µm (to make the hourglass-shaped particle shown in **Figure 4-4**) or 100µm (to make the particles shown in **Figure 4-5**) tall microchannels to achieve a UV light path distinct from the cylindrical light path used previously (**Figure 4-2** and **Figure 4-3**). The high numerical aperture objective causes the incoming UV light to have higher incident angle, which reduces the depth of focus, T_{focus}. This reduction in T_{focus}, coupled with microchannels of increased height, results in a polymerization zone that is no longer a vertical cylinder.
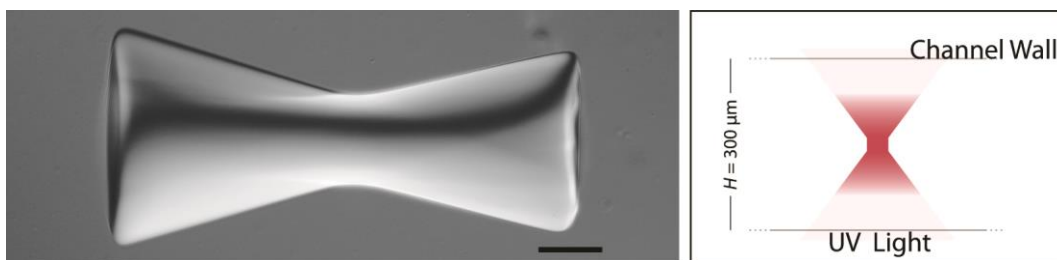
Figure 4-4 An hour-glass shaped particle made in a 300 μm tall microchannel, where the UV light is focused at the mid-plane of the channel height (F = 0.5). Scale bar 50 μm. The right panel shows a schematic diagram of focal plane position relative to the channel height

Figure 4-4 shows an hourglass-shaped hydrogel particle polymerized in a 300 μm tall microchannel with a high numerical aperture objective (N. A. = 0.6). Here the objective focus is placed at the mid-plane of the channel height (right schematic diagram of **Figure 4-4**). The synthesized particle is approximately symmetric about its midpoint because there are no opaque magnetic particles in the precursor to diminish the UV light along the channel height. This particle exhibits a structure with two end lobes and a narrow central region, and well represents the shape of the incoming UV light. With this platform, we can use microchannels of a reduced height of 100 μm, and simply control the objective-to-microchannel distance to obtain a variety of particle shapes (**Figure 4-5**). We define a normalized value for the UV light focal plane relative distance to the bottom of the channel, F, such that F = 1.00 places the focal plane at the top wall of the channel, and F = 0 corresponds to the UV light focused on the bottom substrate. For example, we can bring the objective close to the microchannel such that F = 1.1, to obtain a cone-shaped UV light profile (the right schematic of **Figure 4-5a** shows this focal plane position). This polymerization zone shape produces particles as seen in **Figure 4-5a**. Moving the objective away from the microchannel in a step-wise fashion, such that *F* = 0.80, 0.50, and 0, allows us to synthesize particle shapes seen in **Figure 4-5b**, **c** and **d** respectively.
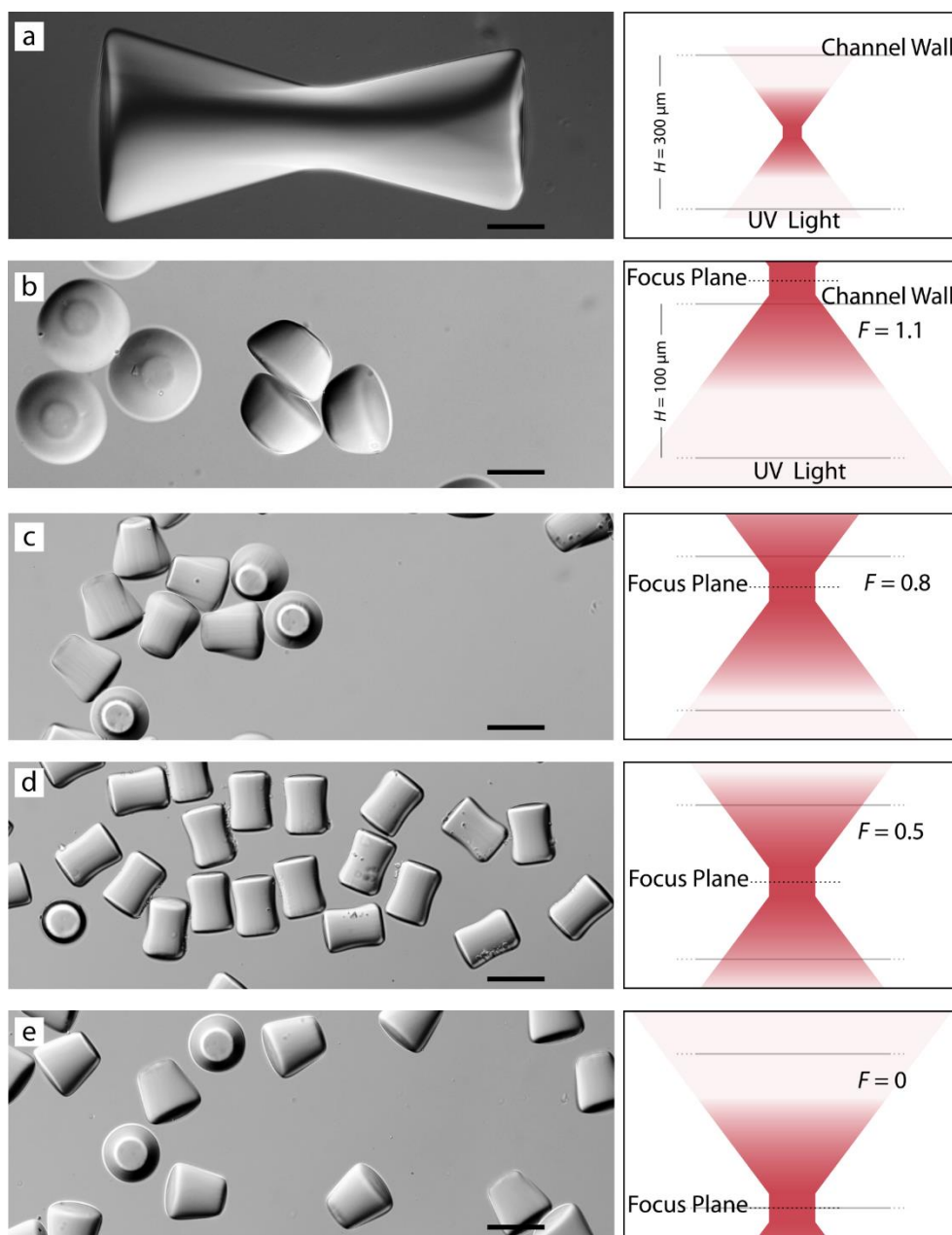
Figure 4-5 Polymeric 3D particles of various shapes, without opaque magnetic material, synthesized using a 40x objective (N. A. = 0.6). **a-d**) Highly uniform 3D particles of different shapes made in 100 µm tall microchannels, while changing the objective-to-microchannel distance to obtain different values of relative focal distance, F. The relative focal distance value, F is 1.10, 0.80, 0.50 and 0 in a, b, c and d, respectively. Scale bars 50 µm. The right panel shows a schematic diagram of focal plane position relative to the channel height in each case.

The schematic diagrams on the right side of **Figure 4-5** show the normalized UV focal plane position, F, in each experiment and simulation. We find a good qualitative agreement

between the simulated particle shapes and our experimental results, as the simulation is able to capture all of the main features of the synthesized particles, including the particle shape and size.

These effects are simply changing the particle shapes from a simple 2D extruded shape to a more complex shape that has high curvature in all dimensions. We can achieve an even higher order of complexity in the morphology of synthesized particles by the combination of tuning of the relative focus plane position F, and adding opaque magnetic nanoparticles to the precursor solution. This creates a gradient of UV light along the channel height, and a non-cylindrical UV light path. UFO shaped magnetic particles (**Figure 4-6**) are synthesized by applying a simple circle photomask (top right inset of **Figure 4-6**). The UV light is focused to $F = -0.2$. A high numerical aperture 40x (N. A. = 0.60) objective is used to achieve a cone shaped UV light path along the channel height. Here the local UV intensity is decreased due to the out-of-focus UV light propagation and the presence of opaque magnetic particles. As a result, the precursor solution is only polymerized in a portion of the channel height. The synthesized particles have a UFO shape due to the diverging cone shape of UV light. The right panel **Figure 4-6** is an SEM image of these UFO shaped particles, after drying, where the particles have stacked into a coherent pattern that is only possible due to their non-spherical 3D shapes.
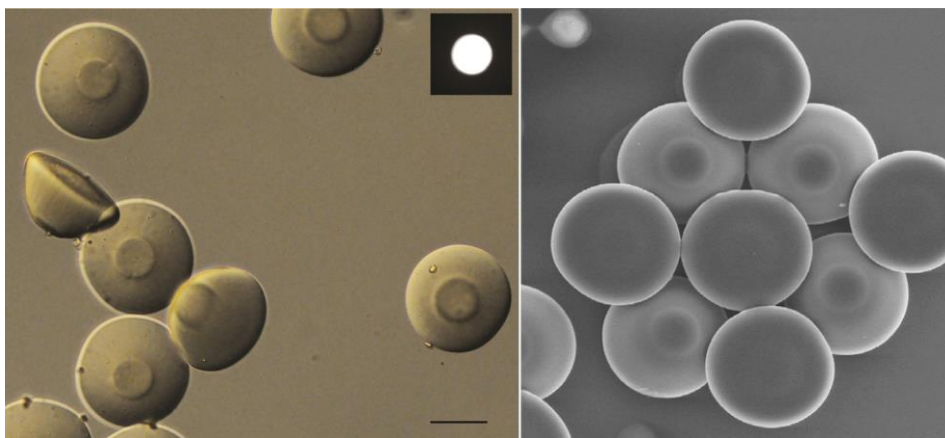
Figure 4-6 Complex-shape magnetic particles synthesized by tuning the UV light focal plane, *F*. Magnetic particles synthesized by focusing the UV light below the bottom surface of the channel such that *F* = -0.2. The right panel shows a SEM image of particles stacked together upon drying. Scale bar 50 μm.

We can also change the photomask pattern to add to the tunability of our technique. For example, by using an alternate photomask pattern (top right inset of **Figure 4-7**), and setting the focal distance F=0, we are able to synthesize 3D particles with high curvature (**Figure 4-7**). The shape of these magnetic particles is controlled by a combination of photomask pattern, magnetic particle concentration, and UV light relative focal plane position, F.
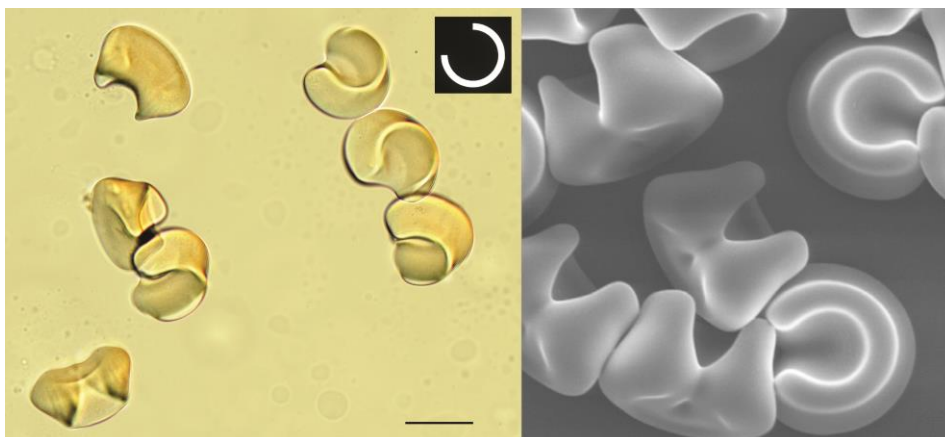
Figure 4-7 Highly curved magnetic particles made by a combination of an alternative photomask pattern (top right inset), the presence of magnetic nanoparticles, and a UV light relative focal distance, *F* = 0. The right panel shows SEM image of the particles. Scale bar 50 um.

4.3 The Effect of Using Discontinuous Photomasks

Exploiting the off-focus UV light propagation using photomasks with disconnected patterns allows for the fabrication of particles with 3D surface features (**Figure 4-8a**) and asymmetric 3D characteristics (**Figure 4-8b**), and branched structures (**Figure 4-9**). The light intensity diminishes as it diverges after passing its focus plane. We use discontinuous photomask patterns, and adjust the pattern spacing, to focus the UV light from a 40x objective (N. A. = 0.6), and create different kinds of diverging light paths along the channel height. We find that, if the transparent parts of a discontinuous photomask pattern are close enough to each other, the UV light going through each hole will constructively interfere, and intensify in specific zones. As a result, polymerization does not only occur directly in-line with the photomask pattern. Rather, the monomer solution also polymerizes in zones where UV light constructively interferes. We take advantage of the out-of-focus overlap of UV light through different photomask holes to make single 3D particles, with a range of 3D features.
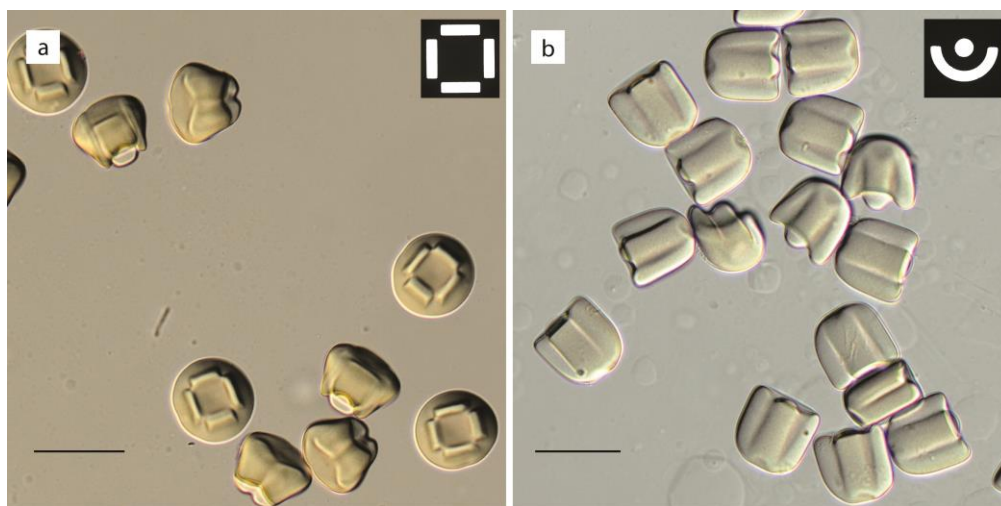
Figure 4-8 A diversity of 3D features, achieved by applying discontinuous photomask patterns, with magnetic precursor solutions, and controlled UV light focal distance F. **a, b)** High curvature

3D particles, with 3D surface features(a) and asymmetric 3D characteristics(b), all synthesized using the method from **Figure 4-6**, albeit modified by the use of disconnected patterns on photomasks. The disconnected photomask patterns here cause non-uniform constructive interference of UV light, which allows polymerization of select regions in the polymer solution. F is -0.2 and 0.2 in a and b respectively. Scale bars 50 um.
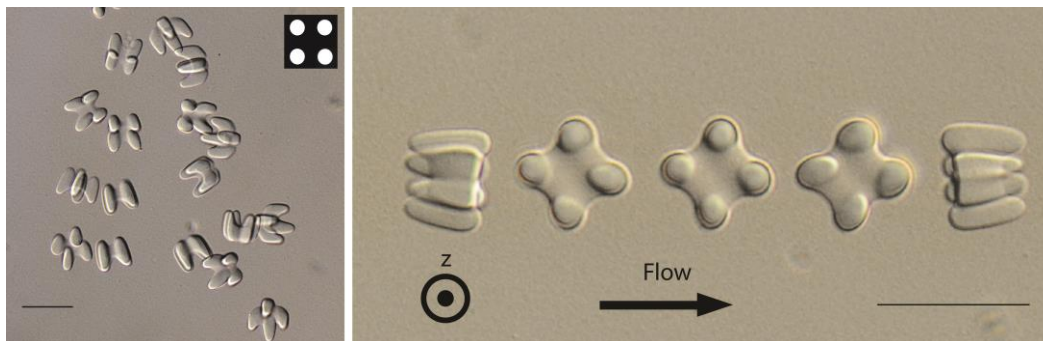
Figure 4-9 Branched structured microparticles synthesized using discontinuous photomasks. The right panel shows a succession of newly manufactured particles with branched legs, moving with the fluid flow in a microchannel. The inset show the photomask that we use to make the corresponding particles. Scale bars 50 μm.

CHAPTER 5

MODELING AND SIMULATION

Previously, Denkurdi et. al (Dendukuri et al. 2007, 818-828) suggested an one-dimensional model that was able to predict the synthesized particle height that obtained from SFL method. We modified that model to consider the two dimensional diffusion of oxygen as well as the radial variation of UV light intensity in our setup. In this model, in addition to the diffusion of oxygen from the top and bottom walls of the channel, we consider diffusion of oxygen molecules from the side walls too. In addition to the particle height, this two dimensional model is able to capture the main features of synthesized particles shapes.

In this chapter, we review the one-dimensional model and their assumptions, and then we describe our modifications to the model.

5.1 Reaction Mechanism

A typical free-radical reaction mechanism (See introduction, **Section** Error! Reference source not found. for more information) is used to drive the reaction kinetics of our polmerization setup.

Table 5-1 Simplified Reaction Mechanism

n	Reaction	Mechanism Step

1	$PI \xrightarrow{hv} R^*$	Photolysis
2	$R^* + M \rightarrow RM^*$	Chain initiation
3	$RM_n^* + M \xrightarrow{k_p} RM_{n+1}^*$	Chain propagation
4	$RM_n^* + RM_m^* \xrightarrow{k_t} RM_n M_m$	Chain termination
5	$RM_n^* + O_2 \xrightarrow{k_o} RM_n OO$	Oxygen inhibition

In the first step, UV light incident on the sample photolysis the initiator molecules (PI) to produce primary radical species (R^*) through a photocleavage mechanism.

In step 2, chain polymerization is initiated when the primary photoinitiator radicals (R^*) react with an unconverted double bond on an oligomer molecule (M). In this model, for simplicity, all the radical species in the process (R^*, R^*M_n) are lumped into the term X. The rate of radical formation can be calculated from step 1 alone, because radicals are formed only in this step. The symbol [M] will represents the concentration of all unconverted double bonds in the precursor solution. In the chain propagation step (step 3), a radical species attacks one molecule of M and forms a larger radical (k_p is the polymerization reaction constant). When two radical species react with each other, they terminate to form a longer chain (step 4); the rate constant for this reaction is k_t. Here only this kind of termination is considered, while other modes of termination are neglected. Molecular oxygen also consumes radicals when they react to form proxy molecules (step 5) with rate constant k_O. The radicals are neutralized when they convert to peroxide species which doesn't attack the monomer molecules.

By working in the focal length of the microscope, we can assume that the UV light path is cylindrical. By which we mean that the area of UV exposure path does not vary along the z direction. In this case, the volumetric rate of absorption by the photoinitiator that yields to free radical formation, r_a is given by:

$$r_a = -\varphi \frac{\varepsilon_1[PI]}{(\varepsilon_1[PI] + \varepsilon_2[OM])} \frac{dI}{dz}$$

Where ε_1 and ε_2 are the extinction coefficients of the photoinitiator and the magnetic nanoparticles, respectively, at a wavelength of 365 nm. [PI] and [OM] represent concentrations of photoinitiator and magnetic nanoparticles, respectively. I is the light intensity and φ is the quantum yield of formation of initiating radicals.

All the radicals envolved in the reactions in this model are lumped into a single term, $[X]$. Based on the reaction scheme, the rate of radical consumption, r_c, is given by

$$r_c = k_t[X]^2 + k_O[X][O_2]$$

with quasi-steady-state approximation

$$r_c = r_a$$

$$[X] = \frac{-k_O[O_2] + \sqrt{(k_O[O_2])^2 + 4r_a k_t}}{2k_t}$$

5.1.1 Species Balance and Solution

In this section, based on the previous work by Dendukuri et al.(Dendukuri et al. 2008, 8547-8556), a 2D axisymmetric mass transport equation for oxygen and monomer is used to obtain expressions for the variation of this species in time and space,

$$\frac{\partial[O_2]}{\partial t} + \nabla \cdot (-D_O \nabla[O_2]) = -k_O[O_2][X] \, ,$$

where $\nabla = [\frac{\partial}{\partial r}, \frac{\partial}{\partial z}]$.

In this equation, $[O_2]$ is the concentration of oxygen, D_O is the diffusivity of oxygen in the precursor solution, k_O is the oxidation reaction constant, and $[X]$ is the concentration of free-radicals. Nondimensionalizing this equation we get

$$\frac{\partial \sigma}{\partial \tau} = \frac{\partial^2 \sigma}{\partial \zeta^2} + \frac{H^2}{\omega_0^2}\frac{\partial^2 \sigma}{\partial \rho^2} - Da_1\sigma\left(-\sigma + \sqrt{\sigma^2 + \alpha I' \exp(-\beta\zeta)}\right), \quad (1)$$

where,

$$\tau = {tD_O}/{H^2} \ , \ \sigma = {[O_2]}/{[O_{2,eqb}]} \ , \ \zeta = {z}/{H} \ , \ \rho = {r}/{H} \ ,$$

$$Da_1 = \frac{k_O^2 H^2 [O_{2,eqb}]}{2k_t D_O} \ , \ \alpha = \frac{4\varphi\varepsilon_1[PI]I_0 k_t}{k_O^2 [O_{2,eqb}]^2} \ , \ \beta = (\varepsilon_1[PI] + \varepsilon_2[OM])H.$$

Here, H is the height of the channel, $[O_{2,eqb}]$ is the equilibrium concentration of oxygen in the precursor solution, k_t is the termination reaction constant, φ is the quantum yield of formation of free-radicals, and $[PI]$ and $[OM]$ are the photoinitiator and opaque materials concentrations respectively. I_0 is the intensity of incoming light, ε_1 is the extinction coefficient of photoinitiator, and ε_2 is the extinction coefficient of opaque materials.

I' is a dimensionless function that represents the variation of UV light intensity in spatial dimensions. This variation does not include the variations caused by absorption of UV light by the opaque materials. The light intensity variation that is related to the absorption by opaque materials and photoinitiator is considered in the $\exp(-\beta\zeta)$ term. The changes that are related to the presence of absorbing particles act separately from the changes in the UV light intensity due to the UV light nature of propagation. As a result, these two terms are separated in the model. For the 1st set of simulations, we consider a radial variation of UV light for the polymerization domain

(chapter 5.2.1) and for the 2nd set of simulations, we consider a variation of UV light in the z direction for the I' term. (See chapter 5.3.)

To solve this PDE, the boundary conditions and initial condition are given by

$\sigma(\rho, \zeta, 0) = 1,$

$\sigma(\rho, 0, \tau) = \sigma(\rho, 1, \tau) = 1,$

$\sigma(\infty, \zeta, \tau) = 1 .$

The concentration of unconverted monomer double bonds in the precursor solutions is given by

$\frac{\partial [M]}{\partial t} = k_p [M][X],$

where k_p is the polymerization reaction constant and $[M]$ is the concentration of monomer in the precursor solution. Because of their relative large sizes, the diffusion of monomer molecules is neglected. Nondimensionalizing this equation results in

$-\frac{\partial \xi}{\partial \tau} = D_{a_2} \xi (-\sigma + \sqrt{\sigma^2 + \alpha\, I' \exp(-\beta \zeta)}),$ (2)

where,

$\xi = \frac{[M]}{[M_0]},\ D_{a_2} = \frac{k_o k_p H^2 [O_{2,eqb}]}{2 k_t D_O}$.

The initial condition for this first order equation is $\xi(\rho, \zeta, 0) = 1$.

Because of the similarity between our setup and the setup of Dendukuri et al.(Dendukuri et al. 2008, 8547-8556), we used the same parameter values for the reaction kinetic constants and equilibrium coefficients. The channel height, H, was 40 μm for the 1st set (see chapter5.2.1) and 100 μm for the 2nd set (see chapter 5.3).

Table 5-2 Parameters values

Parameter	Value	Units	Source
k_p	25	$m^3/(mol\ s)$	(Kızılel, Pérez-Luna, and Teymour 2006, 686-700)
k_t	2520	$m^3/(mol\ s)$	(Kızılel, Pérez-Luna, and Teymour 2006, 686-700)
k_o	5×10^5	$m^3/(mol\ s)$	(Decker and Jenkins 1985, 1241-1244)
ε_1	1.6	$m^3/(mol\ s)$	(Lecamp et al. 2001, 8541-8547)
$[O_{2,eqb}]$	1.5	mol/m^3	(Goodner and Bowman 2002, 887-900)
φ	0.6	1	(Lecamp et al. 2001, 8541-8547)
H	40 (for the 1st set), 100 (for the 2nd set)	40 μm 100 μm	Measured
$[PI]$	329	mol/m^3	Measured
I_0	5×10^{-2}	$E/(m^2\ s)$	Provided by the manufacturer

Table 5-3 Values of nondimensional numbers

Parameter	Value
α	3×10^{-7}
$\beta*$	0.2 (for the 1st set), 0.01 (for the 2nd set)
Da_1	4×10^9 (for the 1st set), 3×10^{10} (for the 2nd set)
Da_2	2×10^5 (for the 1st set), 1×10^6 (for the 2nd set)

* Because of the difficulty in the calculation of β, we considered β as a fitting parameter for our simulations. The assumed β values are in the same order of magnitude as they were calculated in previous models.($\beta = 0.1$)(Suh et al. 2011, 13813-13819).

5.2 Non-uniformity of the UV light

We believe the 3D features of our particles arises from the non-uniformity of polymerizing light. In the previous studies, the UV light was considered to be homogenous along its path. In our modification to the model, we consider the following factors that results in the non-uniformity of light in our setup. In this section, we mention our assumptions about the causes of non-uniformity of light and then we theorize and quantify these factors in order to include them into the model.

5.2.1 Calculation of Depth of Focus

In the previous model by dendukurdi et. al, the polymerization zone was considered to be in the depth of focus of the microscope. This will result in a cylindrical UV exposure path. However, this is not globally true. In our setup, the polymerization zone is not always cylindrical. The reason is that we believe some of the polymerization is occurred out of focus of the UV light propagation path.

Historically, depth of focus and depth of field are used interchangeably. However, these two terms represents different meanings. Depth of field (DOF) is the distance between the closest and farthest objects that appear sufficiently sharp in an image. Depth of focus is the tolerance of the placement of the image plane (exposure plane) relative to the lens. In other words, depth of focus is the distance over which the image plane can be displaced while a single object plane remains in acceptably sharp focus.

In the stop-flow lithography setup, the UV light comes from a single object plane, and polymerization occurs in the vicinity of image plane. Zeiss microscopy has provided a separate formula to calculate depth of field and depth of focus:

$$\text{Depth of field, } T_{Field}(\mu m) = \frac{1000}{7*NA_{objective}*Mag_{total}} + \frac{\lambda(\mu m)}{2*NA_{Objectibe}^2},$$

$$\text{and depth of focus, } T_{Focus}(\mu m) = \frac{1000*Mag_{objective}}{7*NA_{objective}*Mag_{total}} + \frac{\lambda(\mu m)*Mag_{objective}^2}{2*NA_{Objectibe}^2},$$

where $N.A.$ is the numerical aperture of the objective and λ is the wavelength of light. Mag_{total} and $Mag_{objective}$ are the magnification factors of the microscope and the objective, respectively

Table 5-4 Calculated Depth of Field and Depth of Focus using Zeiss formula

N.A.	Objective	Depth of Field (μm)	Depth of Focus (μm)
0.3	10x	49	136
0.4	20x	19	53
0.5	20x	15	42
0.6	40x	6	19

For making the particles seen in **Figure 4-2**, we used a 20x objective with N.A. = 0.4 and the channel height was 40 μm. That means the polymerization occurred in the depth of focus of the microscope. However, for making the particle seen in **Figure 4-3** and **Error! Reference source not found.**, we used a 40x objective with N. A. = 0.6. The channel height was 300 μm for **Figure 4-3**, and 100 μm for **Error! Reference source not found.**. So the polymerization zone is bigger than the depth of focus, and some of the polymerization is occurred out of focus.

5.2.2 Radial variation of cylindrical UV light path

The radial variation of UV light in flow lithography methods is already known. This variation is more significant where smaller photomasks are implemented(Dendukuri et al. 2006, 365-369). For considering this variation in our model, we plotted the light profile along several diameters of an exposed photomask on a solution of 0.001 (v/v) Rhodamine B (Sigam Aldrich) in water. We nondimensionalized the light intensity values by the maximum light intensity and the diameter of the photomask by channel height. We repeated this procedure for five times on two different diameter photomask holes and averaged the values. Then we fitted the collected data using the HoO2 equation. The HoO2 is a modification on general Sellemeier equation.

The general Sellemeier equation is

$$n(\lambda)^2 - 1 = \sum_i \frac{A_i \lambda^2}{\lambda^2 - \lambda_i^2} .$$

The HoO2 equation that is used for fitting the intensity data versus radial distance from the center of UV exposure path in this model is:

$$I'(\rho)^2 = A + B\rho^2 + \frac{C\rho^2}{\rho^2 - D^2} ,$$

where I' is the nondimensionized intensity and ρ is nondimensionized radius. Our UV exposure data fitted HoO2 equation well when we calculated it for small photo58mask sizes (10 μm and 20 μm):

Table 5-5 Fitting data of fitting UV intensity plots on HoO2 equation using 10 μm photomask

Objective	A	B	C	D	SSQABS	RMSE	R²
10x N.A. = 0.3	1.00E+00	1.75E+02	2.76E+04	1.25E+01	1.13E-02	0.010	0.984
20x N.A. = 0.4	9.85E-01	1.60E+02	2.97E+03	4.21E+00	3.88E-02	0.020	0.984

20x N.A. = 0.5	9.93E-01	4.60E+00	1.75E+02	3.99E+00	4.36E-03	0.006	0.996
40x N.A. = 0.6	9.86E-01	7.87E+02	2.96E+03	-1.91E+00	7.83E-02	0.028	0.946

Table 5-6 Fitting data of fitting UV intensity plots on HoO2 equation using 20 μm photomask

Objective	A	B	C	D	SSQABS	RMSE	R^2
10x N.A. = 0.3	8.97E-01	2.05E+00	6.82E+00	2.00E+00	6.90E-02	0.019	0.914
20x N.A. = 0.4	9.77E-01	1.09E+01	1.99E+01	1.38E+00	1.95E-02	0.010	0.982
20x N.A. = 0.5	9.84E-01	7.46E+00	1.12E+01	1.24E+00	7.25E-03	0.006	0.993
40x N.A. = 0.6	9.82E-01	6.28E+00	2.84E+00	5.80E-01	2.07E-02	0.010	0.978

In **Figure 4-2** , we used these fitted data for UV light radial variation. We used a 10 μm photomask, a 20x (N. A. = 0.4) in a 40 μm height microchannel. As an example, for this objective and photomask, the images shown in **Figure 5-1** are obtained:

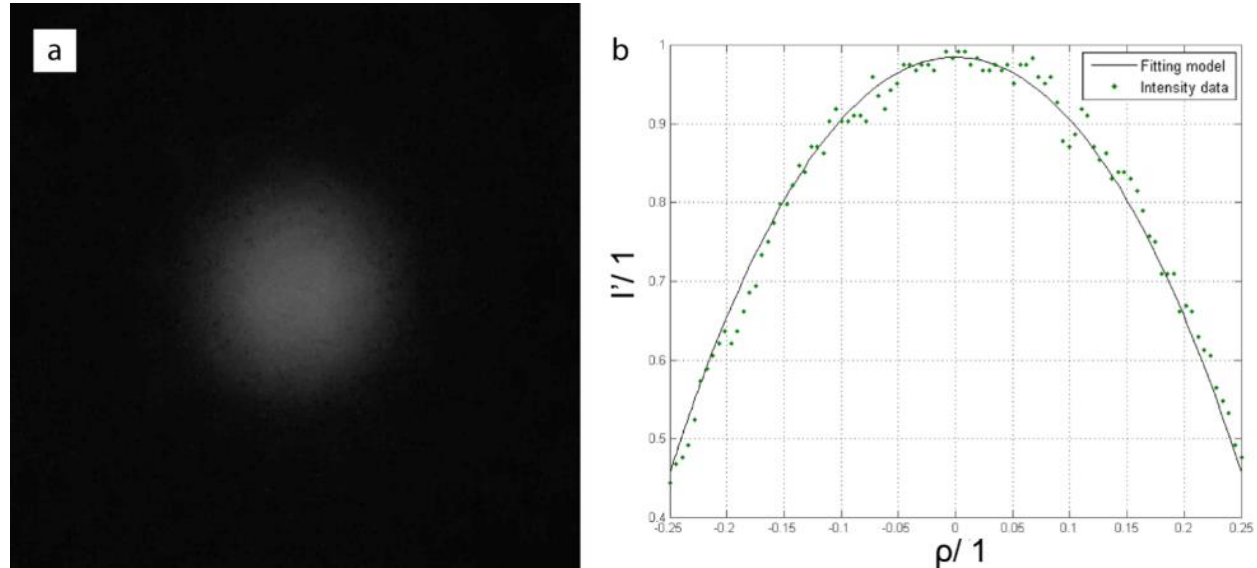**Figure 5-1** Modeling of radial UV intensity variations using HoO2 equation**.** a) An gray-scaled image of Rhodamine-B solution illumination when exposed to UV light coming from a 20x (N.A. = 0.4) object through a 10 μm circle photomask. b) Comparison between the UV light relative intensity in radial direction to HoO2 model that is used in the simulations as the UV profile in the radial direction.

5.3 2D axisymmetric modeling and simulation of magnetic particle synthesis assuming cylindrical UV path

The surface plots in **Figure 5-2** shows the normalized oxygen concentration profile, ($\sigma = [O_2]/[O_{2,eqb}]$), in the cross section of the channel, where $[O_2]$ and $[O_{2,eqb}]$ are the precursor solution's present and the equilibrium oxygen concentrations, in a PDMS environment, respectively. **Figure 5-2** compares different formation of bullet shaped particle simulation results using the fitting function for radial variation of UV light, and not considering that variation (the simulation result shown in **Figure 5-2b** corresponds to the bullet shaped particles shown in **Figure 4-2**). In these contours the critical monomer conversion contour $1 - \xi = 0.02$ ($\xi = [M]/[M_0]$), is depicted with the white line. $[M]$ and $[M_0]$ are the present and initial monomer concentrations of the precursor solution, respectively. Solidification of the precursor takes place where monomer conversion is higher than a critical value, $1 - \xi > 0.02$.(Andrzejewska 2001, 605-665) The region within the white contours shows monomer conversion above the threshold value, thus giving the predicted particle shape. We use this 2D model to simulate the 3D particle shape because the system is axisymmetric about the *z*-axis. The length scales are non-dimensionalized with respect to channel height such that $\rho = r/H$ and $\zeta = z/H$. Having symmetry about the z-axis also allows us to impose a symmetric boundary condition along the vertical centerline of the polymerization domain, and only solve the model for half of the cross-section domain. We find that our 2D model is able to capture both the curvature and size of the bullet-shape particles we synthesized in our experiments.
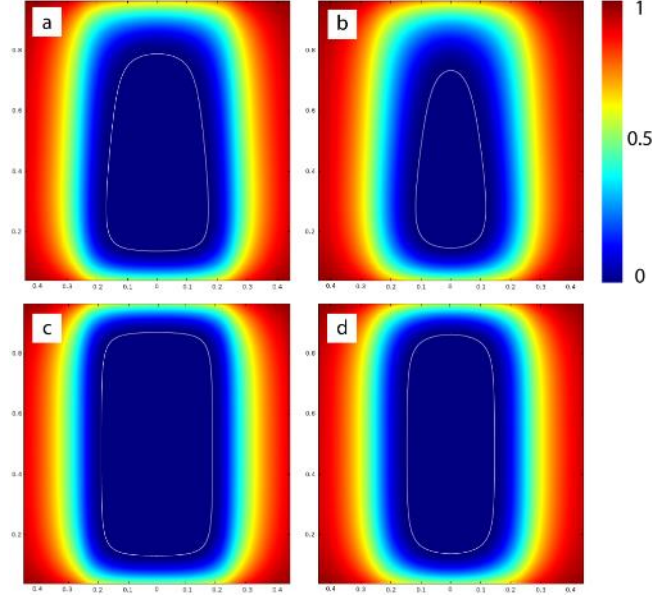
Figure 5-2 Numerical simulations of the normalized oxygen concentration and monomer conversion in the cross section of the channel, with the axial variation of UV light (**a**), the axial and radial variation of UV light (**b**), no variation of UV light (**c**), and the radial variation of UV light (**d**). The surface plot represents the oxygen concentration ($\sigma = [O_2]/[O_{2,eqb}]$) and the white line represents the critical monomer conversion, $1 - \xi = 0.02, (\xi = [M]/[M_0])$. The region enclosed by the white contour line has a monomer conversion factor above the threshold level such that the precursor solution solidifies into a gel. Thus, the white contour line also gives a prediction of the particle shape.

5.4 2D axisymmetric Modeling and Simulation of polymeric particle synthesis assuming non-cylindrical UV path

As we mentioned in the previous sections there two main important factors that change the intensity of light in the reaction domain. The light intensity changes due to absorption of light by the species present in the precursor solution, and also it changes due to the complex nature of its propagation from a UV source with large wavelengths range through a photomask and an objective. These two factors act separately and allow us to separate their effects on light intensity in our modeling.

According to Beer's law, the absorption effect can be expressed by the following equation, assuming that the photoinitiator and magnetic nanoparticles absorb UV light independently,

$$\frac{\partial I}{\partial z}\bigg|_{Constant\ A} = -(\varepsilon_1[PI] + \varepsilon_2[OM])I(z).$$

On the other hand, when the light is traveling in its out of focus region, the cross section area that light travels through is changing all the time,

$$A = \pi r^2.$$

We assµme a simple geometry for the light propagation path based on the fact that light is either diverging or converging with an contact angle, θ, when its off the focused path. Based on the assumed geometry of the problem, for those regions we have,

$$r = (FH - z)\tan\theta.$$

Here, F is the normalized value for the UV light relative focal plane to bottom of the channel distance that is described in the main text. F can be changed easily by changing the microscope stage to objective distance, and is an important particle shape-defining parameter. Changing F values will result in different polymerization zones, and various particle shapes can be achieved. (See **Figure 4-5**)

$$\frac{dA}{dz} = 2\pi(\tan\theta)^2(z - FH).$$

When absorption is not considered we have the conservation of energy of UV beam. So,

$$IA = I'A' = constant = c,$$

$$A\partial I + I\partial A = 0 \qquad ,$$

and $\frac{\partial I}{\partial A}_{Constant\ z} = -\frac{I}{A} = -\frac{I}{\pi(FH-z)^2\,(\tan\theta)^2}$.

replacing the values,

$\frac{\partial I}{\partial z}_{no\ absorption} = -\frac{2I(z)}{(z-FH)}$.

by separating the variables and taking the integral we have,

$\int_{I_{in}}^{I}\frac{dI}{I(z)} = \int_0^z\left(-\frac{2}{(z-FH)}\right)dz$,

and $= I_{in}\frac{F^2H^2}{(z-FH)^2}$.

I_{in} is the incoming intensity of the UV light that enters the bottom of the channel. If the incoming UV light is focused, we can measure it and replace the value. But if the incoming UV light is not focused, we have to calculate the value based on our assumption as follows,

$I_{focused}A_{focused} = I_{in}A_{unfocused}$.

assuming the focused photomask diameter is ω_0,

$I_{focused}\pi\frac{\omega_0^2}{4} = I_{in}\pi r_{in}^2$,

or

$I_{in} = \frac{\omega_0^2}{4F^2H^2(tan\theta)^2}I_{focused}$,

thus, $I' = \frac{\omega_0^2}{4(z-FH)^2(tan\theta)^2}$.

Surface plots of the simulated dimensionless oxygen concentration, σ, and the critical monomer conversion contours, $1 - \xi = 0.02$, of the polymerization region are plotted in

Figure 5-3. The simulated critical monomer conversion contours (white lines) represent the predicted particle shapes. These simulation results correspond to the polymeric particles shown in **Figure 4-5**.
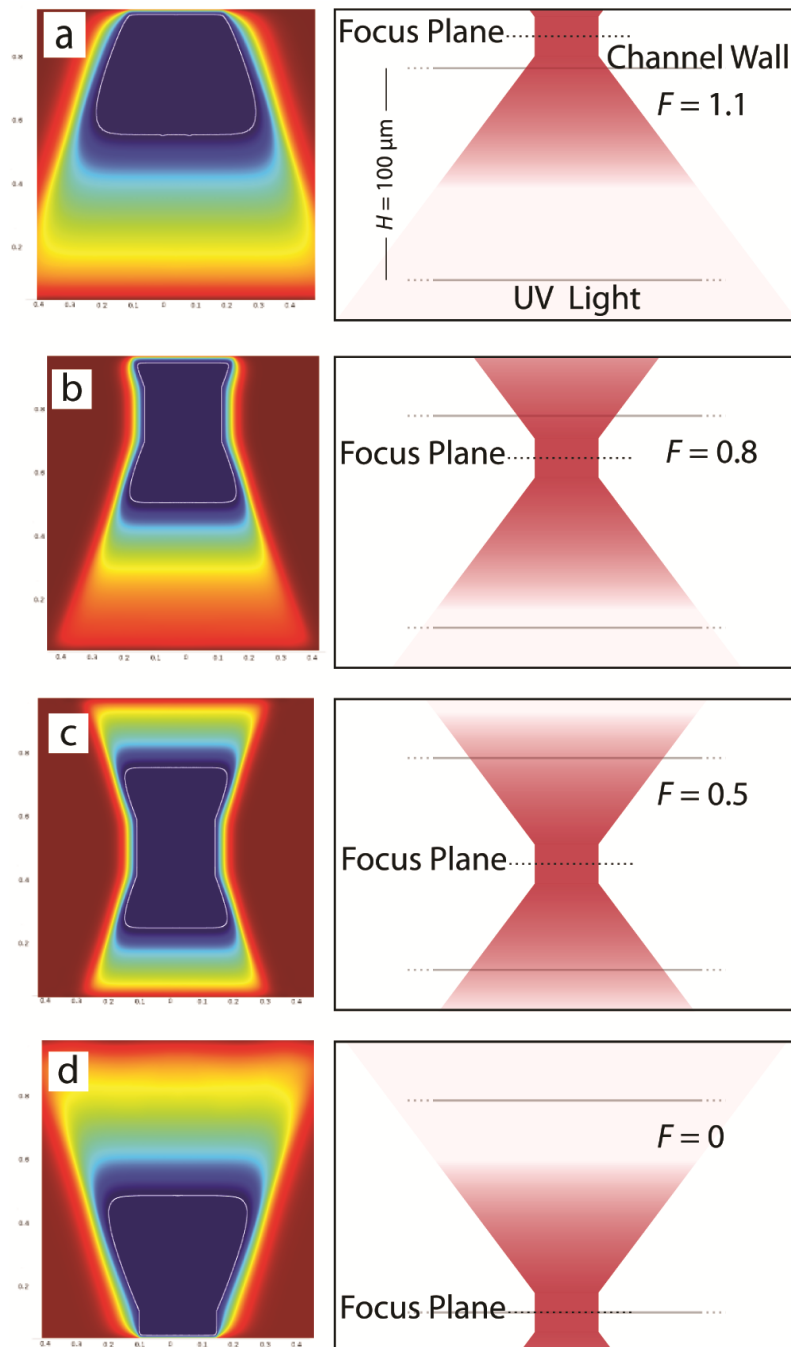
Figure 5-3 Simulation results of out of focus polymerization of polymeric particles. The simulated oxygen concentration, σ, on a surface plot, and the simulated critical monomer conversion contour, $1\,\xi = 0.02$, as the white line which gives predicted particle shapes in each case. The relative focal distance value, F is 1.10, 0.80, 0.50 and 0 in a, b, c and d, respectively. The right panel shows a schematic diagram of focal plane position relative to the channel height in each case.

We did not consider the radial variation of UV light in this case because we observed it to be negligible. The reasons behind this assumption is that first of all, the photomask size is bigger (50 μm was the radius of photomask for synthesizing the particle shown in **Figure 4-2**, and 30 μm for **Figure 4-5**). As we mentioned before chapter 5.2.2, as the photomask size increases, the radial variation of UV light diminishes to a slight edge effect with the uniform intensity profile along the center region. The second reason for not considering the radial variation is that the precursor solution contains little absorbing materials and thus the radial variation the incoming UV light does not significantly affect the formation of particles. The final reason is that the synthesized particles shown in **Figure 4-5** show no curvature in the radial direction.

Figure 5-4 Intensity profiles of illuminated Rhodamin-B solutions in water when exposed to UV light through a 20x (N.A. = 0.4) objective using different photomask sizes. Here, the length scale is nondimensionalized with respect to photomask size ($\rho' = r/(radius\ of\ photomask)$). This plot shows that with increasing the photomask size, the radial variation of UV light becomes less significant.
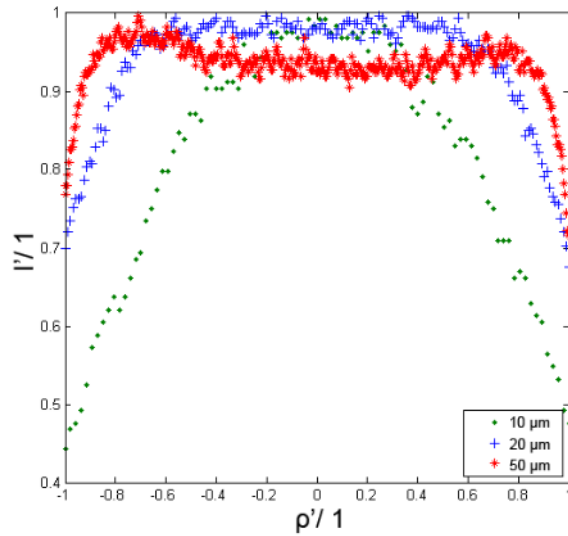
5.4.1 Diverging angle

The range of angles over which the objective can emit light is determined by the nature of light and the numerical aperture (N.A.) of the objective. Regularly, the angle of the maximum cone of light that can exit the objective is calculated by

$$NA = nsin\theta,$$

or

$$\theta = Arcsin\left(\frac{NA}{n}\right). \qquad (3)$$

n is the index of refraction of the medium that fills the objective (n = 1 for air).

Laser beams typically have a Gaussian profile in which θ is the divergence of the beam. In this kind of profile, the beam does not have the sharp edges of a cone. Instead, the intensity reduces gradually away from the center of the beam. In our polymerization setup, the angle calculated from Eq. 3 is 0.645 radians. However, when we exposed a 300 µm tall channel to make the particle shown in **Figure 4-4**, the synthesized particle lobes had an angle of 0.245 radians. Because of the oxygen inhibition from the sides of the reaction zone, and also due to the small edge effect of the UV light intensity profile in the radial direction using a 50 µm circle photomask, (shown in **Figure 5-4**) we concluded that the angle of exposure is in the range of 0.645 and 0.245 radians. We decided to use a mean value between these two angels, θ = 0.445, as the diverging angle in our simulations. This set of simulations show that a wide range of particles with 3D features can be easily made in a 2D channel by only changing the microscope objective to stage distance in order to set relative focus plane distance, F, value. These simulations capture the general feature of the synthesized particle. They also show other important shape defying factors, such as the strength of the objective, (N. A. of the objective) that changes the angle of 3D features of the

particle, and channel height, which is important not only to set the height of the synthesized particles, but also in capturing the off focus regions of UV light propagation.
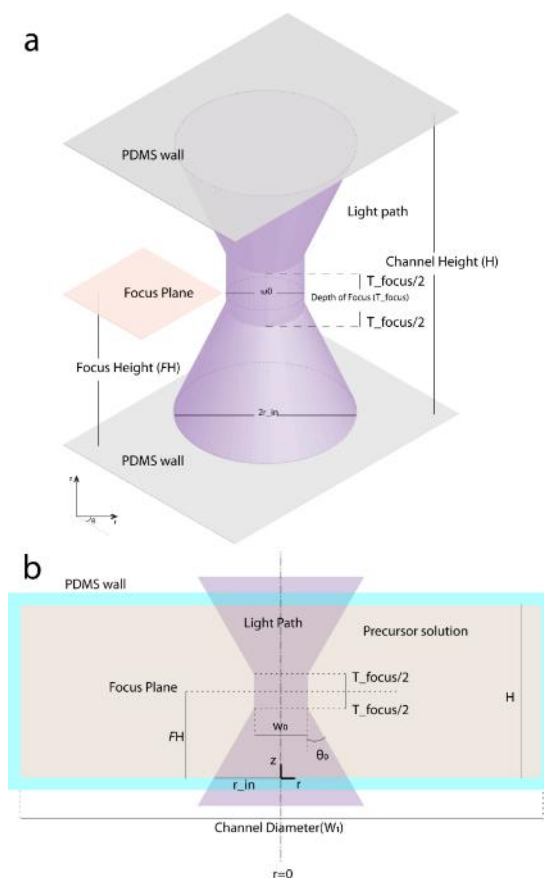
Figure 5-5 schematic diagrams of the assµmed geometry. **a-b**) 3D (a) and 2D (b) schematic of the assumed light path in our setup. Here, the purple domain shows the light path. T_{focus} is the depth of focus that is calculated using the Zeiss formula. H is the channel height, w_0 is the illuminated photomask size, F is the relative focal distance, θ_0 is the contact angle of the light.

5.5 Solution strategy

We solved equations 1 and 2 simultaneously using the coefficient form of Comsol Multiphysics. The solver we used was Pardiso, and the maximum number of iterations was set to 400 with free time stepping. For plotting the critical monomer conversion contour, we plotted the $\xi = 0.98$ contour, which represents a 0.02 conversion of the monomer molecules that is considered

the threshold conversion at which the precursor solution solidifies. The radius of channel was considered to be 5ρ. (5 is the ratio of channel width to channel height in our setup. Changing this value in the range of one to infinity does not considerably affect the solution, because far from the polymerization zone, the concentration of oxygen is always near $[O_{2,eqb}]$, or $\sigma = 1$.)

CHAPTER 6

CONCLUSIONS

The achievements of this research project can be summarized in the following points:

- We have developed a novel microfluidic-based method that is able to manufacture **FUNCTIONAL 3D** microparticles with **BRANCHED STRUCTURES** and **HIGH CURVATURE** in a **SIMPLE 2D** microchannel.

- We have introduced a numerical model that can predict the main features of the resulting particle **shapes**.

6.1 Recommendations

The following recommendations are proposed for future studies:

- Quantitative characterization of control parameters such as precursor opacity, UV intensity and UV intensity profile must be followed to optimize the process and generate particles with desirable shapes.

- We showed that photomasks with discontinuous patterns can create particles with branched structures. Future studies are required to characterize the effects of array, spacing and size of the discontinuous patterns on the development of particle curvatures. .

References

Andrzejewska, E. 2001. Photopolymerization kinetics of multifunctional monomers. *Progress in Polymer Science* 26 (4): 605-65.

Barua, S., J. W. Yoo, P. Kolhar, A. Wakankar, Y. R. Gokarn, and S. Mitragotri. 2013. Particle shape enhances specificity of antibody-displaying nanoparticles. *Proceedings of the National Academy of Sciences of the United States of America* 110 (9): 3270-5.

Bong, K. W., D. C. Pregibon, and P. S. Doyle. 2009. Lock release lithography for 3D and composite microparticles. *Lab on a Chip* 9 (7): 863-6.

Brahim, Sean, Dyer Narinesingh, and Anthony Guiseppi-Elie. 2002. Polypyrrole-hydrogel composites for the construction of clinically important biosensors. *Biosensors and Bioelectronics* 17 (1–2) (1): 53-9.

Bryant, Stephanie J., Charles R. Nuttelman, and Kristi S. Anseth. 2000. Cytocompatibility of UV and visible light photoinitiating systems on cultured NIH/3T3 fibroblasts in vitro. *Journal of Biomaterials Science, Polymer Edition* 11 (5): 439-57.

Champion, J. A., Y. K. Katare, and S. Mitragotri. 2007. Particle shape: A new design parameter for micro- and nanoscale drug delivery carriers. *Journal of Controlled Release* 121 (1-2): 3-9.

Chaterji, S., I. K. Kwon, and K. Park. 2007. Smart polymeric gels: Redefining the limits of biomedical devices. *Progress in Polymer Science* 32 (8-9): 1083-122.

Chung, B. G., K. H. Lee, A. Khademhosseini, and S. H. Lee. 2012. Microfluidic fabrication of microengineered hydrogels and their application in tissue engineering. *Lab on a Chip* 12 (1): 45-59.

Chung, S. E., Y. Jung, and S. Kwon. 2011. Three-dimensional fluidic self-assembly by axis translation of two-dimensionally fabricated microcomponents in railed microfluidics. *Small* 7 (6) : 796-803.

Chung, S. E., W. Park, H. Park, K. Yu, N. Park, and S. Kwon. 2007. Optofluidic maskless lithography system for real-time synthesis of photopolymerized microstructures in microfluidic channels. *Applied Physics Letters* 91 (4):525-532.

Cushing, M. C., and K. S. Anseth. 2007. Materials science. hydrogel cell cultures. *Science (New York, N.Y.)* 316 (5828): 1133-4.

Das, M., H. Zhang, and E. Kumacheva. 2006. Microgels: Old materials with new applications. *Annual Review of Materials Research* 36: 117-42.

Decker, Christian, and Aubrey D. Jenkins. 1985. Kinetic approach of oxygen inhibition in ultraviolet-and laser-induced polymerizations. *Macromolecules* 18 (6): 1241-4.

Dendukuri, D., and P. S. Doyle. 2009. The synthesis and assembly of polymeric microparticles using microfluidics. *Advanced Materials* 21 (41): 4071-86.

Dendukuri, D., S. S. Gu, D. C. Pregibon, T. A. Hatton, and P. S. Doyle. 2007. Stop-flow lithography in a microfluidic device. *Lab on a Chip* 7 (7): 818-28.

Dendukuri, D., P. Panda, R. Haghgooie, J. M. Kim, T. A. Hatton, and P. S. Doyle. 2008. Modeling of oxygen-inhibited free radical photopolymerization in a PDMS microfluidic device. *Macromolecules* 41 (22): 8547-56.

Dendukuri, D., D. C. Pregibon, J. Collins, T. A. Hatton, and P. S. Doyle. 2006. Continuous-flow lithography for high-throughput microparticle synthesis. *Nature Materials* 5 (5): 365-9.

Drury, J. L., and D. J. Mooney. 2003. Hydrogels for tissue engineering: Scaffold design variables and applications. *Biomaterials* 24 (24): 4337-51.

Dubinsky, Stanislav, Hong Zhang, Zhihong Nie, Ilya Gourevich, Dan Voicu, Martin Deetz, and Eugenia Kumacheva. 2008. Microfluidic synthesis of macroporous copolymer particles. *Macromolecules* 41 (10): 3555-61.

Flory, and P J. 1953. *Principles of polymer chemistry*Cornell University Press.

Franke, T., S. Braunmuller, L. Schmid, A. Wixforth, and D. A. Weitz. 2010. Surface acoustic wave actuated cell sorting (SAWACS). *Lab on a Chip* 10 (6): 789-94.

Garstecki, P., M. J. Fuerstman, H. A. Stone, and G. M. Whitesides. 2006. Formation of droplets and bubbles in a microfluidic T-junction - scaling and mechanism of break-up (vol 6, pg 437, 2006). *Lab on a Chip* 6 (5): 693.

Gent, Alan N. 2001. *Engineering with rubber: How to design rubber components*Hanser Verlag.

Georges, Veregin, and Homer Kazmeier. 1993. Free radical polymerization. *Macromolecules* 26 : 5316.

Ghosh, Pulak K., Vyacheslav R. Misko, Fabio Marchesoni, and Franco Nori. 2013. Self-propelled janus particles in a ratchet: Numerical simulations. *Physical Review Letters* 110 (26): 268301.

Glotzer, S. C., and M. J. Solomon. 2007. Anisotropy of building blocks and their assembly into complex structures. *Nature Materials* 6 (8): 557-62.

Goodner, Michael D., and Christopher N. Bowman. 2002. Development of a comprehensive free radical photopolymerization model incorporating heat and mass transfer effects in thick films. *Chemical Engineering Science* 57 (5): 887-900.

Hageman, HJ. 1985. Photoinitiators for free radical polymerization. *Progress in Organic Coatings* 13 (2): 123-50.

Helgeson, M. E., S. C. Chapin, and P. S. Doyle. 2011. Hydrogel microparticles from lithographic processes: Novel materials for fundamental and applied colloid science. *Current Opinion in Colloid & Interface Science* 16 (2): 106-17.

Hoare, Todd R., and Daniel S. Kohane. 2008. Hydrogels in drug delivery: Progress and challenges. *Polymer* 49 (8) (4/15): 1993-2007.

Hwang, D. K., D. Dendukuri, and P. S. Doyle. 2008. Microfluidic-based synthesis of non-spherical magnetic hydrogel microparticles. *Lab on a Chip* 8 (10): 1640-7.

International Union of Pure and Applied Chemistry. Commission on Macromolecular Nomenclature, Richard G. Jones, and International Union of Pure and Applied Chemistry. Commission on Macromolecular Nomenclature. 2009. *Compendium of polymer terminology and nomenclature*. Cambridge: RSC Pub.

Jang, J. H., D. Dendukuri, T. A. Hatton, E. L. Thomas, and P. S. Doyle. 2007. A route to three-dimensional structures in a microfluidic device: Stop-flow interference lithography. *Angewandte Chemie-International Edition* 46 (47): 9027-31.

Kaiser, W., and C. G. B. Garrett. 1961. Two-photon excitation in CaF_2: Eu^{2+}. *Phys.Rev.Lett.* 7 (6): 229-31.

Kanazaki, Takahiro, and Tetsuo Okada. 2012. Two-dimensional particle separation in coupled acoustic-gravity-flow field vertically by composition and laterally by size. *Analytical Chemistry* 84 (24): 10750-5.

Kızılel, Seda, Víctor H. Pérez-Luna, and Fouad Teymour. 2006. Mathematical model for Surface-Initiated photopolymerization of poly (ethylene glycol) diacrylate. *Macromolecular Theory and Simulations* 15 (9): 686-700.

Kost, J., J. Wolfrum, and R. Langer. 1987. Magnetically enhanced insulin release in diabetic rats. *Journal of Biomedical Materials Research* 21 (12): 1367-73.

KRATOCHVfL, P. 1996. Glossary of basic terms in polymer science.

LaFratta, C. N., J. T. Fourkas, T. Baldacchini, and R. A. Farrer. 2007. Multiphoton fabrication. *Angewandte Chemie-International Edition* 46 (33): 6238-58.

Lattuada, Marco, and T. Alan Hatton. 2011. Synthesis, properties and applications of janus nanoparticles. *Nano Today* 6 (3): 286-308.

LaVan, D. A., D. M. Lynn, and R. Langer. 2002. Moving smaller in drug discovery and delivery. *Nature Reviews.Drug Discovery* 1 (1): 77-84.

Laza, S. C., M. Polo, A. A. R. Neves, R. Cingolani, A. Camposeo, and D. Pisignano. 2012. Two-photon continuous flow lithography. *Advanced Materials* 24 (10): 1304-8.

Lecamp, L., P. Lebaudy, B. Youssef, and C. Bunel. 2001. Influence of UV radiation wavelength on conversion and temperature distribution profiles within dimethacrylate thick material during photopolymerization. *Polymer* 42 (21): 8541-7.

Lee, K. J., J. Yoon, and J. Lahann. 2011. Recent advances with anisotropic particles. *Current Opinion in Colloid & Interface Science* 16 (3): 195-202.

Lee, S. A., S. E. Chung, W. Park, S. H. Lee, and S. Kwon. 2009. Three-dimensional fabrication of heterogeneous microstructures using soft membrane deformation and optofluidic maskless lithography. *Lab on a Chip* 9 (12): 1670-5.

Li, Fan, David P. Josephson, and Andreas Stein. 2011. Colloidal assembly: The road from particles to colloidal molecules and crystals. *Angewandte Chemie International Edition* 50 (2): 360-88.

Li, Yuhui, Guoyou Huang, Xiaohui Zhang, Baoqiang Li, Yongmei Chen, Tingli Lu, Tian Jian Lu, and Feng Xu. 2013. Magnetic hydrogels and their potential biomedical applications. *Advanced Functional Materials* 23 (6): 660-72.

Lötters, JC, W. Olthuis, PH Veltink, and P. Bergveld. 1997. The mechanical properties of the rubber elastic polymer polydimethylsiloxane for sensor applications. *Journal of Micromechanics and Microengineering* 7 (3): 145.

Medeiros, S. F., A. M. Santos, H. Fessi, and A. Elaissari. 2011. Stimuli-responsive magnetic particles for biomedical applications. *International Journal of Pharmaceutics* 403 (1–2) (1/17): 139-61.

Merkel, T. J., K. P. Herlihy, J. Nunes, R. M. Orgel, J. P. Rolland, and J. M. DeSimone. 2010. Scalable, shape-specific, top-down fabrication methods for the synthesis of engineered colloidal particles. *Langmuir* 26 (16): 13086-96.

Nisisako, Takasi, Toru Torii, Takanori Takahashi, and Yoichi Takizawa. 2006. Synthesis of monodisperse bicolored janus particles with electrical anisotropy using a microfluidic Co-Flow system. *Advanced Materials* 18 (9): 1152-6.

Odian, George G. 2007. *Principles of polymerization*

Pamme, N., and C. Wilhelm. 2006. Continuous sorting of magnetic cells via on-chip free-flow magnetophoresis. *Lab on a Chip* 6 (8): 974-80.

Panda, P., K. P. Yuet, T. A. Hatton, and P. S. Doyle. 2009. Tuning curvature in flow lithography: A new class of Concave/Convex particles. *Langmuir* 25 (10): 5986-92.

Park, Tae Gwan, and Allan S. Hoffman. 1994. Deswelling characteristics of poly(N-isopropylacrylamide) hydrogel. *Journal of Applied Polymer Science* 52 (1): 85-9.

Qiu, Y., and K. Park. 2012. Environment-sensitive hydrogels for drug delivery. *Advanced Drug Delivery Reviews* 64: 49-60.

Reyes, Darwin R., Dimitri Iossifidis, Pierre-Alain Auroux, and Andreas Manz. 2002. Micro total analysis systems. 1. introduction, theory, and technology. *Analytical Chemistry* 74 (12): 2623-36.

Rolland, J. P., B. W. Maynor, L. E. Euliss, A. E. Exner, G. M. Denison, and J. M. DeSimone. 2005. Direct fabrication and harvesting of monodisperse, shape-specific nanobiomaterials. *Journal of the American Chemical Society* 127 (28): 10096-100.

Saunders, B. R., and B. Vincent. 1999. Microgel particles as model colloids: Theory, properties and applications. *Advances in Colloid and Interface Science* 80 (1): 1-25.

Seemann, Ralf, Martin Brinkmann, Thomas Pfohl, and Stephan Herminghaus. 2012a. Droplet based microfluidics. *Reports on Progress in Physics* 75 (1): 016601.

Seemann, Ralf, Martin Brinkmann, Thomas Pfohl, and Stephan Herminghaus. 2012b. Droplet based microfluidics. *Reports on Progress in Physics* 75 (1): 016601.

Shin, M. K., S. I. Kim, S. J. Kim, S. Y. Park, Y. H. Hyun, Y. Lee, K. E. Lee, et al. 2008. Controlled magnetic nanofiber hydrogels by clustering ferritin. *Langmuir : The ACS Journal of Surfaces and Colloids* 24 (21): 12107-11.

Shogenji, R., Y. Kitamura, K. Yamada, S. Miyatake, and J. Tanida. 2004. Bimodal fingerprint capturing system based on compound-eye imaging module. *Applied Optics* 43 (6): 1355-9.

Shum, H. C., A. R. Abate, D. Lee, A. R. Studart, B. G. Wang, C. H. Chen, J. Thiele, R. K. Shah, A. Krummel, and D. A. Weitz. 2010. Droplet microfluidics for fabrication of non-spherical particles. *Macromolecular Rapid Communications* 31 (2): 108-18.

Sooklal, Kelly, Leo H. Hanus, Harry J. Ploehn, and Catherine J. Murphy. 1998. A blue-emitting CdS/Dendrimer nanocomposite. *Advanced Materials* 10 (14): 1083-7.

Spearing, S. M. 2000. Materials issues in microelectromechanical systems (MEMS). *Acta Materialia* 48 (1): 179-96.

Sugioka, Koji, and Ya - Cheng. - *Femtosecond laser processing for optofluidic fabrication*- The Royal Society of Chemistry.

Suh, S. K., K. W. Bong, T. A. Hatton, and P. S. Doyle. 2011. Using stop-flow lithography to produce opaque microparticles: Synthesis and modeling. *Langmuir* 27 (22): 13813-9.

Synytska, Alla, Rina Khanum, Leonid Ionov, Chokri Cherif, and C. Bellmann. 2011. Water-repellent textile via decorating fibers with amphiphilic janus particles. *ACS Applied Materials & Interfaces* 3 (4): 1216-20.

Takeuchi, Shoji, Piotr Garstecki, Douglas B. Weibel, and George M. Whitesides. 2005. An axisymmetric Flow-Focusing microfluidic device. *Advanced Materials* 17 (8): 1067-72.

Tibbitt, M. W., and K. S. Anseth. 2009. Hydrogels as extracellular matrix mimics for 3D cell culture. *Biotechnology and Bioengineering* 103 (4): 655-63.

Tsai, S. S. H., I. M. Griffiths, and H. A. Stone. 2011. Microfluidic immunomagnetic multi-target sorting - a model for controlling deflection of paramagnetic beads. *Lab on a Chip* 11 (15): 2577-82.

Tsai, S. S. H., J. S. Wexler, J. D. Wan, and H. A. Stone. 2011. Conformal coating of particles in microchannels by magnetic forcing. *Applied Physics Letters* 99 (15).

Walther, Andreas, Martin Hoffmann, and Axel HE Müller. 2008. Emulsion polymerization using janus particles as stabilizers. *Angewandte Chemie* 120 (4): 723-6.

Whitesides, G. M., and B. Grzybowski. 2002. Self-assembly at all scales. *Science* 295 (5564): 2418-21.

Xu, JH, SW Li, J. Tan, YJ Wang, and GS Luo. 2006. Preparation of highly monodisperse droplet in a T-junction microfluidic device. *AICHE Journal* 52 (9): 3005-10.

Xu, Jing, Dominica H. C. Wong, James D. Byrne, Kai Chen, Charles Bowerman, and Joseph M. DeSimone. 2013. Future of the particle replication in nonwetting templates (PRINT) technology. *Angewandte Chemie International Edition* 52 (26): 6580-9.

Xu, S., J. Zhang, C. Paquet, Y. Lin, and E. Kumacheva. 2003. From hybrid microgels to photonic crystals. *Advanced Functional Materials* 13 (6): 468-72.

Zhang, Y. L., Q. D. Chen, H. Xia, and H. B. Sun. 2010. Designable 3D nanofabrication by femtosecond laser direct writing. *Nano Today* 5 (5): 435-48.

Ziv-Polat, O., M. Topaz, T. Brosh, and S. Margel. 2010. Enhancement of incisional wound healing by thrombin conjugated iron oxide nanoparticles. *Biomaterials* 31 (4): 741-7.